Mass Loss From Evolved Stars in Elliptical Galaxies

Joel R. Parriott and Joel N. Bregman

Department of Astronomy, University of Michigan, Ann Arbor, MI 48109

jbregman@umich.edu

ABSTRACT

Most of the X-ray emitting gas in early-type galaxies probably originates from red giant mass loss and here we model the interaction between this stellar mass loss and the hot ambient medium. Using two-dimensional hydrodynamic simulations, we adopt a temperature for the ambient medium of $3 \quad 10^6$ K along with a range of ambient densities and stellar velocities. When the stellar velocity is supersonic relative to the ambient medium, a bow shock occurs, along with a shock driven into the stellar ejecta, which heats only a fraction of the gas. Behind the bow shock, a cool wake develops but the fast flow of the hot medium causes Kelvin-Helmholtz instabilities to grow and these fingers are shocked and heated (without radiative cooling). Along with the mixing of this wake material with the hot medium, most of the stellar ejecta is heated to approximately the temperature of the hot ambient medium within 2 pc of the star. With the addition of radiative cooling, some wake material remains cool ($< 10^5$ K), accounting for up to 25% of the stellar mass loss. Less cooled gas survives when the ambient density is lower or when the stellar velocity is higher than in our reference case. These results suggest that some cooled gas should be present in the inner part of early-type galaxies that have a hot ambient medium. These calculations may explain the observed distributed optical emission line gas as well as the presence of dust in early-type galaxies.

Subject headings: galaxies: ISM | -cooling flows | -X-rays: galaxies | -stars: mass loss

1. Introduction

The observed metallicities of hot gas in early-type galaxies disagree with elementary predictions. The source of the hot galactic gas is expected to be the mass lost by evolved stars. The main contribution to the gas mass is from giant stars and planetary nebulae

and this gas initially has the velocity of the parent star. As this material collides with the mass lost from other stars or with the hot ambient medium within the galaxy, the mass loss material is shocked to a temperature corresponding to the velocity dispersion of the stars in the galaxy (review by Mathews & Brighenti 2003). If this were the only heating mechanism, the gas would have the velocity dispersion temperature and a metallicity of the stars. The metallicity of early-type galaxies have been measured, and for galaxies near L^*, the metallicity is approximately solar within $R_e/2$ (Trager et al. 2000).

However, there is a second source of metals, due to the occurrence of Type Ia supernovae in these galaxies (Turatto, Cappellaro, & Benetti 1994). The mass of Fe from these supernovae is many times greater than that in the mass lost from giant stars, so the net result is that the Fe abundance of the hot ISM in early-type galaxies should be 3–10 times the solar value (Renzini et al. 1993; Brighenti & Mathews 2005). The other prediction is that the heating by the supernovae should raise the gas temperature above that due only to the velocity dispersion of the stars. While the gas temperature is indeed elevated above the velocity dispersion temperature (e.g., Brown & Bregman 1998), the metallicities are far from these predicted values, lying near the Solar value in the more X-ray luminous early-type galaxies (Athey 2003; Humphrey & Buote 2006).

One modification to the model is that gas from the surrounding environment has fallen into the galaxy, diluting the metallicity of the gas (Mathews & Brighenti 2003). This might predict a sharp radial metallicity gradient, with more dilution in the outer parts and less in the inner part of the galaxy, where there is a lower ratio of the stellar mass loss rate to the density of the group or cluster medium. Such a gradient is not generally detected in the X-ray observations of the hot gas (Athey 2003; Humphrey & Buote 2006).

The issue of external gas accretion should be relatively unimportant in galaxies that are thought to be driving galactic winds. Partial or total galactic winds are the leading explanation for the X-ray poor early-type galaxies, whose gas content is an order of magnitude less than their X-ray bright counterparts. In these systems, the supernova heating may be enhanced, thereby driving the galactic wind. In this picture, David et al. (2006) estimate that the Fe abundance would be an order of magnitude above the Solar value. However, observations of X-ray faint early-type galaxies shows that the Fe abundance in the hot gas is lower than the X-ray bright ellipticals, with typical values that are 0.3 of the Solar value (Irwin et al. 2006). Evidently, there is a metallicity problem: the metals in the mass lost by stars is not effectively mixed into the host ISM of these galaxies.

This metallicity problem has been recognized for over a decade (e.g., Fujita et al. 1996, 1997) and a resolution to the problem may be that the metals do not fully mix into the ISM (Mathews 1990; Brighenti & Mathews 2005). One aspect of this is that not all stars

have the same metallicity. As these authors point out, higher metallicity gas radiates more effectively, so it might cool to $T \sim 10^4$ K if the cooling time is shorter than the heating and mixing timescale. This would produce a bias against high-metallicity gas becoming part of the hot ISM. Estimations for the magnitude of the effect have been calculated, which involve spherically symmetric bubbles and shocks that propagate into the mass lost from stars. However, the more realistic situation will have some important differences. For the typical condition where the star is losing mass as it moves through the ambient ISM at a few hundred km s^{-1}, there will be a bow shock in front of the star. As the shocked gas flows by the stellar mass loss, it will create a wake with strong velocity gradients. Kelvin-Helmholtz instabilities are likely to develop between the rapidly flowing shocked gas and the stellar mass loss, and this will lead to shocking of the cooler gas and mixing between the two components. These processes are difficult to estimate accurately, so we have undertaken a series of numerical fluid dynamical calculations to study the process by which stellar mass loss interacts with the hot ambient medium.

2. Computational Methodology

The gas dynamics code used in this work is based upon the highly accurate Piecewise Parabolic Method (PPM) of Colella & Woodward (1984). The choice of PPM as the numerical scheme for these simulations is based upon the hydrodynamics that are expected to be important in our physical problem. PPM is robust, and its high spatial and temporal accuracy (discontinuity capturing) capabilities make it a natural choice, since vortex mixing and shock heating are expected to be the key mechanisms for transforming the cold stellar ejecta into hot ambient gas. The implementation of PPM used here (Blondin & Lufkin 1993) contains improvements that make it more suitable for the geometry and boundary conditions found in our problem. The PPM scheme of Colella & Woodward (1984) was written to operate on a grid defined by the volume $V(r)$ rather than the position r (remap step) or mass coordinate m (Lagrangian step), thus rendering the interpolation Cartesian in V. In this way, curvilinear geometry can be incorporated without having to correct for coordinate singularities. However, a volume-based interpolation does not accurately capture the solution on a reflecting symmetry boundary, where the velocity u is generally linear in r, not $V(r)$. So even though the original PPM scheme can account for curvilinear geometries, the cumulative truncation error for advection of a velocity interpolated on the volume coordinate near a symmetry axis is first-order in r/r. Blondin & Lufkin (1993) demonstrated that the PPM-LR scheme retains greater accuracy near coordinate singularities when using interpolations in r (or) instead of $V(r)$. Three relatively simple modifications to the original scheme are required for improved accuracy in both the radial and azimuthal coordinates.

We began with the serial version of the code of Blondin & Lufkin (1993), known as VH–1 and written for distribution by the Virginia Institute of Theoretical Astrophysics (VITA) Numerical Astrophysics Group. This is a two-dimensional code that we use in spherical polar coordinates. The VH–1 code implements PPM as a Lagrangian hydrodynamic step coupled with a remap onto the original fixed Eulerian grid (referred to as PPM–LR). This scheme combines the advantages of Lagrangian and Eulerian methods by solving the fluid equations in Lagrangian mode and then remapping the dynamical variables back to the fixed Eulerian grid. Because the physics and the coordinate transformation are solved for separately. If the remap and the Lagrangian scheme are each third order, the entire solution will be third order.

The original VH–1 code was modified in a few significant ways before it could be used to address our problem. First, we introduced optically thin radiative losses, which was implemented by the operator splitting method outside of the Riemann solver after each full time step; for further discussion of the VH–1 code and the modifications, see Parriott (1998). While this represents a loss of self-consistency with the gas dynamics, it is a much used and validated method of including heating and/or cooling. We use the local, time-independent collisional ionization equilibrium cooling function, $_N(T)$, of (Sutherland and Dopita 1993). These tables cover a temperature range of 10^4K $10^{8.5}$K, and a large metallicity range of [Fe=H] = 3:0 +0:5.

The routine employs an implicit scheme, the secant method, to calculate the energy (or equivalently, the pressure) lost in one time step. The computational load incurred by an implicit method is justified by its ability to minimize the small errors introduced when removing energy from the system. In practice, the code uses interpolated values from a table of radiative cooling function values as a function of temperature, and iterates toward a value for the change in temperature for each cell. The iteration is carried out a maximum of twelve times, or until the fractional temperature change is less than one part in a thousand, $T=T < 10^{-3}$. A new temperature is calculated for each cell, and the pressure is changed accordingly (in this case via the ideal gas equation of state):

$$p = \frac{k_b T}{m_p}; \text{ where } T = \frac{1}{4 m_p k_b} {}_N t: \qquad (1)$$

Finally, we tested the output of the cooling routine using a flat cooling function and a single temperature grid with no inflow or outflow. The temperature drop over the time taken by N time steps had to exactly match analytical expectations.

The second change was to the computational grid. We maintained the regular nature of the 2D spherical polar grid, but created an unequal spacing of grid cells. The outermost

radius is 25 pc and at the innermost radius, 0.01 pc, the stellar surface is not resolved. The radial length of the cells increase by a factor of 1.01 per cell, which creates much higher radial resolution in the inner grid. This growth dictates an outermost cell 36 times longer than the innermost cell when using 360 radial cells. This inner resolution is important since it is the region where the instabilities begin to grow. We also found it important in helping the lower energy density material flow into the grid from the inner boundary without encountering non-physical negative pressures in several cells near the boundary. Because most of the important structure develops in the wake along the downstream symmetry polar axis, we also increased the azimuthal resolution by a factor of 10 for the cells in that region (Figure 1). This is accomplished by calculating a beginning angular cell size, decreasing that size by an order of magnitude and forming 100 azimuthal cells at that resolution. The remaining cells fill in the rest of the radians to complete the grid.

The third modification concerns the boundary procedures for the 2D axisymmetric spherical polar domain. The outer boundary of the grid needed to have an inflow boundary condition on the left side for the hot, fast ambient wind, and an outflow only condition on the right side for the gas to leave the grid. Since the public VH-1 code treats the entire outer boundary as one boundary with one condition, we split the boundary in half. A particular 1D radial sweep uses the inflow condition if its angular theta value lies in the second quadrant ($\cos(\theta) < 0$), or uses the outflow condition if its theta is in the first quadrant ($\cos(\theta) \geq 0$). The inflow boundary condition was set by zero-gradient fixed values for the pressure, density, velocity, and derived total energy of the hot, fast ambient wind. We also used a zero-gradient outflow condition, but added a pressure condition which set the minimum pressure of the outflow ghost zones at the fixed inflow pressure value. While this change is unnecessary for supersonic flows, it helps to reduce the influence of sound waves hitting the boundary for sub-sonic flows, and prevents any pressure buildup near the outflow boundary. A dissertation on boundary procedures for fluid dynamics found that boundary conditions, no matter how well-conceived and physically elegant, can never eliminate all of the problems incurred at outer boundaries, and one should make the boundary as far away as practically possible (Body 1992).

The boundaries along the upwind and downwind symmetry axis were implemented with reflecting boundary conditions. The density and pressure gradients are set to zero at the boundary, and the sign of the velocity is changed.

The inner boundary adjacent to the upstream symmetry axis was troublesome in that a small amount of material representing the stellar outflow could work its way upstream further than the bulk of the ram pressure confined stellar wind (see Figure 2). Although VH-1 includes the non-Cartesian improvements to the spatial interpolation routine, it does

not completely eliminate the errors (Blondin & Lufkin 1993). The restriction of axisymmetry makes this axis a favorable place for such errors to grow, even though the improved interpolation is implemented (Blondin 1998). This behavior in VH-1 was noted by Dinge (1997), where it occurred in his simulations of proto-globular cluster clouds. After a number of attempts to fix this problem, we conclude that it is difficult to remove without moving to a three-dimensional code. However, the error that it introduces does not appear to affect the behavior and evolution of the wake, which is orders of magnitude more massive and energetically important.

The final change to the serial version of VH-1 involved a test and correction if the pressure of a given cell becomes negative during the remap step. This happens when the kinetic energy u^2 and thermal energy NkT of a cell are similar in magnitude, so that small errors in the velocity can drive the derived thermal pressure negative ($p_{derived} \propto (E_{thermal} - E_{kinetic})$). We repair the problem cell by computing a new pressure from the average temperature of the adjacent two cells in the direction of the current sweep. We are injecting energy into the grid using this method, but the amounts of energy are very small, so the effects on the general flow are minor.

The public version of VH-1 was a serial code, which for our problem, would have taken too long to produce results for the computers available at the time of this work. Consequently, we carried out a significant programming effort to produce a parallel implemention of VH-1, the details of which were a significant part of a doctoral dissertation (Parriott 1998). The parallel implementation and code testing are also described in the dissertation.

3. Simulations of Stellar Mass Loss in a Hot Galactic Medium

There are certain common properties of all of the simulations, which involve a hot, fast ambient medium gas flowing past a mass-losing star that is fixed at the origin of the axisymmetric grid. The hot, fast ambient medium gas flows from left to right across the grid with velocity $v_{amb} = \ ?$, density n_{amb}, and temperature T_{amb}. The pressure is determined from the ideal gas law. The outer boundaries have fixed in flow procedures on the left and fixed out flow procedures on the right with a check to make sure that the out flow pressure does not exceed the in flow pressure. The inner boundary represents a surface beyond the actual stellar surface with fixed in flow procedures. The gas in flow from this boundary is the cold, slowly moving stellar wind, with a strictly outward radial velocity of v_{ejecta}, density, n_{ejecta}, and temperature T_{ejecta}. The mass loss rate that this corresponds to will be a constant value for all runs, and for all time. The exception to this is a non-steady state simulation of a planetary nebula-like mass loss episode (to be discussed elsewhere). The axial grid

boundaries implement a simple reflecting boundary condition. A cartoon of this scenario, after a bow shock and wake have formed, is shown in Figure 3. Every simulation is run from a physical time of 0 years to 3 10^6 years. The calculated wake flow time of 8 10^5 years, so we conservatively allow one million years for the flow to become quasi-steady-state. Any steady-state averaging is done for simulation times between one and three million years. There are 10 runs: five in the 2-D parameter space of (v_{amb}, n_{amb}), and five more at the same v_{amb} and n_{amb} with radiative cooling turned on.

3.1. The Fiducial Simulation

We find it useful to define a reference or fiducial simulation, against which other simulations are compared. The parameters used for the fiducial simulation represent average physical quantities near the effective radius for a typical intermediate luminosity elliptical galaxy. This first simulation does not include the effects of radiative cooling. We will examine in detail the important physical processes that drive the heating and cooling of the stellar ejecta, given a particular set of input parameters. Once we have established our analysis for this fiducial run, it will serve as a reference point for examining the influence of varying the ambient conditions, and radiative cooling. The parameters for this (FDFV) and subsequent simulations are shown in Table 1. Each simulation is run with a single metallicity radiative cooling routine turned off and on. A particular model is designated by a series of four or five letters, where F stands for the fiducial values, so for the range of density, fiducial density conditions are designated FD, high density regions HD, and low density regions as LD. This is followed by two letters describing the flow velocity, where the fiducial velocity is FV, high velocity is HV, and low velocity is LV. The detailed densities and velocities associated with these runs are given in Tables 1, 2. Simulations that also have cooling are designated with a C as the last character. So a simulation with the higher density, with the fiducial velocity and with radiative cooling is designated HDFVC.

In this fiducial simulation, the hot gas velocity is v_{amb} = 350 km s^{-1}, which corresponds to a one-dimensional velocity dispersion $_?$ 200 km s^{-1} from the relationship $v = \sqrt{3}$. This velocity dispersion is representative of a low to intermediate luminosity galaxy (Canizares, Fabbiano, & Trinchieri 1987; Matsumoto et al. 1997). The density of the gas is n_{amb} = 10^{-3} cm^{-3}, which is a typical value for the galaxy. Since we have used values typical of intermediate L_X galaxies, we set the temperature of the X-ray gas T_{amb} = 3 10^6 K 0.3 keV. These parameters lead to a gas moving slightly supersonically, with a Mach number M 1.4 for = 5/3, and a pressure nT = 3 10^3 K cm^{-3}. This pressure is typical of the gas in the middle to outer regions of an elliptical galaxy.

The stellar mass loss rate that we use here ($\dot{M}_{star}$ $10^{-7} M_\odot$ yr^{-1}), and for the other simulations, is a time-weighted average value for the red giant and asymptotic giant branch stages of stellar evolution for a solar-type star (Reimers 1975; Frank, Balick, & Riley 1990). The input parameters for the ejecta inflow boundary that result in this rate are $v_{ejecta} = 35$ km s^{-1}, and $n_{ejecta} = 1$ cm^{-3}, with a temperature $T_{ejecta} = 10^4$ K. These are all average quantities for a stellar wind at $r = 0.1$ pc. A simple mass flux estimate at $r = 0.1$ pc gives $\dot{M}_{star}$ 4.8 $10^{-8} M_\odot$ yr^{-1}. This mass loss rate is half the rate that we want from the inner boundary, but given these input values we obtain an actual calculated mass flux near $\dot{M}_{star}$ $10^{-7} M_\odot$ yr^{-1}. This is due to high pressure gradients near the boundary that affect the inflow.

As material begins to flow into the ambient medium from the boundary representing the stellar outflow, a contact discontinuity and bow shock are formed. The ambient flow imparts momentum to the stellar ejecta that pushes it into a downstream wake that is in pressure equilibrium with the ambient gas. There are a few fluid instabilities that occur in this situation. When a shock wave impulsively accelerates a density interface, small amplitude perturbations grown and, in the non-linear regime, one fluid component penetrates the other. The conditions appropriate for this Richtmyer-Meshkov instability appear to occur at the forward contact surface of the bow shock, a situation common for all simulations. Further downstream in the flow, there is a cool wake with a relatively rapidly flowing hotter and lower density medium. This situation is unstable to the growth of Kelvin-Helmholtz instabilities. As these instabilities travel down the wake, vortices are formed, further mixing the two gases. In addition, cool material that extends or detaches from the wake or head region can collide and shock with the fast low-density material flowing by. Within these interactions, the conditions for Rayleigh-Taylor instabilities are sometimes established, and this instability also helps to mix the wake gas with the ambient material. Because of these processes, the amount of cold (T 10^4 K) gas is greatly reduced by the time the wake exits the grid in this non-radiative cooling run. The entire grid for this simulation after a quasi-steady state flow has been established with a fully formed bow shock and complex wake is shown in Figure 4.

A bow shock is formed upstream from the stellar inflow boundary since the ambient gas is mildly supersonic. The standoff distance between the inner boundary and the vertex of the bow shock and contact discontinuity is consistent with theoretical expectations. The standoff distance from a mass losing star is found by balancing the ram pressures of the ambient medium and stellar wind, $_{amb} v_{amb}^2 = _{ej} v_{ej}^2$, where $_{amb}$, v_{amb}, $_{ej}$, and v_{ej} are the mass density and velocity of the ambient medium and ejecta at the contact, respectively. Solving for the standoff distance from the center of the star r_0 given that $_{ej} \propto r^{-2}$, yields (Baranov, Krasnobaev, & Kulikovskii 1971; Dyson 1975; Wilkin 1996):

$$r_0 = \left(\frac{\dot{M}_{star} v_{ej}}{4 \pi \rho_{amb} v_{amb}^2} \right)^{1/2} . \quad (2)$$

The simulation typically places the contact discontinuity near $r_0 \approx 0.4$ pc (see Figure 5), which is almost precisely the calculated value of $r_0 \approx 0.4$ pc, given input values of $\dot{M}_{star} = 10^{-7} M_\odot$ yr^{-1}; $v_{amb} = 350$ km s^{-1}; $\rho_{amb} = 2 \times 10^{-27}$ g cm^{-3}; $v_{ej} = 35$ km s^{-1} which are for a boundary at $r = 0.1$ pc. The precise location of the shocks varies with time as large instabilities peel off the contact and present an ejecta region with a temporarily larger effective cross-section.

The main function of the bow shock is to thermalize the ambient gas as the ambient flow imparts momentum to the ejecta, pushing it into a wake. The early formation of this bow shock is shown in Figure 6. Shock heating from the bow shock and contact discontinuity is the mechanism invoked by the standard theory to locally thermalize 100% of the stellar material to the velocity dispersion temperature. However, the simulation makes it clear that these shocks are not heating all the ejecta, and do not appear to be the main heating mechanism.

3.2. The Role of Kelvin-Helmholtz Instabilities

The relative tangential velocity difference between the stellar mass loss and the ambient medium causes Kelvin-Helmholtz (hereafter KH) instabilities to develop. In the linear regime the growth rate of the KH instability η_{KH}, with the wave number $k = 2\pi/\lambda$, is given by (e.g., Lamb 1945):

$$\eta_{KH} = k \left(\frac{\rho_{amb} \rho_{ej}}{(\rho_{amb} + \rho_{ej})^2} (v_{amb} - v_{ej})^2 \right)^{1/2} , \quad (3)$$

where ρ_{amb}, v_{amb}, ρ_{ej}, and v_{ej} are now the mass density and tangential velocity of the shocked ambient medium and ejecta, respectively. The e-folding growth time $\tau_{KH} \equiv 1/\eta_{KH}$ of modes for the present case with $\rho_{amb} \gg \rho_{ej}$ and $v_{amb} \gg v_{ej}$ is approximately given by:

$$\tau_{KH} \approx \frac{\lambda}{2\pi} \left(\frac{\rho_{ej}}{\rho_{amb}} \right)^{1/2} \frac{\lambda}{v_{amb}} , \quad (4)$$

where λ is the length scale of growing mode.

In considering the growth of KH modes, we note that modes with below the numerical resolution of the grid and algorithm are suppressed. The grid resolution at the contact surface at the head of the flow is r 0.01 parsecs, while the elongated cells half the distance down the high-resolution wake region are r 0.1 parsecs, 0.01 parsecs. These modes might be important in the evolution of the wake material, but we cannot address them. We will calculate e-folding growth times for typical conditions present in the contact discontinuity and wake, where KH instabilities are seen to form and grow. These times will be shown to typically be 100 times shorter than the flow time (i.e. the time for the wake to be advected off the grid). Since the flow is quasi-steady state after roughly 8 10^5 years, we assume that any results from times later than this are typical of the flow evolution. The numbers used for the current analysis were taken from the grid state at a simulation time of 10^6 years.

We will first examine the conditions for the contact discontinuity at the leading edge of the ejecta-ambient collision. Figure 5 shows mass density and temperature contours for the region including the vertex of the bow shock, the main contact discontinuity, and the first growing KH instabilities. The temperature map also shows the upstream leakage of a small amount of cold gas along the reflecting symmetry axis due to unavoidable numerical errors (see above). Since we are interested in the steady state wake flow, the influence of this axis error should be minimal. The bow shock is not visible on the density map since the density drop across it is very small, but its location is indicated by the short white line. The black arrow represents the line where the data were extracted to make the density and velocity plots in Figure 7. The data were extracted from this line because the velocities ambient gas and the ejecta are almost totally parallel to each other and tangential to the discontinuity at this point, which is a necessary condition for the velocities in Equation 4. After substituting what appears to be a typical base length for some beginning instabilities as the length scale 0.2 pc, and the other relevant values ($_{amb}$ 3 10^{27} g cm ^{3}; $_{ej}$ 5 10^{25} g cm ^{3}; and v_{amb} 155 km s ^{1}) into the linear Equation 4, we obtain $_{KH}$ 3000 years for the leading edge flow. It should be noted that the "ambient" values used here were actually the post-shock gas values since that is the fluid actually at the contact discontinuity (inner shock). The flow time is simply found by dividing the radius of the grid by the speed of the wake v_{ej}, so that $_{flow,wake}$ 8 10^5 years. As stated above, $_{KH}$ $_{flow,wake}$, so there is ample time for these instabilities to form. It should be noted that the modes that form do so with a very high degree of spatial and temporal accuracy, given an inner cell size of order 0.01 pc on a side, and a Courant time step that is typically $t_{Courant}$ 5 years. The longer modes will take longer to form and we see that the larger instabilities present themselves further downstream, and these less frequent modes appear to do a great deal of wake mixing.

The second KH instability measurements are from a typical region in the downstream wake from at the same simulation time. Instead of the clear two-shock structure seen in the head region, the wake consists of the cold ejecta material with significant mixing taking place through the many KH instabilities and the vortices that they form. This unstable colder material is in pressure equilibrium with the ambient medium, but it is still separated from the hot gas by a more broad discontinuity that we will call a shear layer. Figure 8 shows mass density and temperature contours for this region of the wake, as well as the line where data were extracted. As stated above, since the flow is quasi-steady state, we can assume that the place where we have extracted data to be average and typical for the wake flow. The mass density and velocity profiles are shown in Figure 9. The data used in the KH time calculations are taken on each size of the full shear layer. Since the wake and ambient flows are almost entirely in the X-direction, with the exception of vortices, the velocity in that direction is appropriate for the KH calculations. The density contrast between the wake and the hot gas is not as large as at the head contact discontinuity, so we need to use Equation 3 to find KH growth times rather than using Equation 4. Substituting the relevant wake parameters for the ejecta values ($_{amb}$ 2 10^{27} g cm ^{3}; $_{wake}$ 3 10^{26} g cm ^{3}; and v_{amb} 300 km s ^{1} ; v_{wake} 30 km s ^{1}), and with a longer empirically determined length scale of 1 pc, we obtain $_{KH}$ 3000 years for the wake region. The longer length scales in the wake region compensate for the smaller density contrasts compared to the head region, so that $_{KH}$ is approximately the same for both regions. This time scale is over 100 times shorter than the flow time, so the instabilities have plenty of time to grow before they are advected off the grid. The long modes take a longer time to form, and we see large instabilities in the wake that we do not see in the head region, presumably because they do not have time to form before being advected downstream.

These simulations show that Kelvin-Helmholtz (KH) instabilities have ample time and resolution to grow in all areas of the ejecta-ambient gas interface. The instabilities, and the vortices that form directly downwind of them, are the primary mechanisms for heating by mixing the cold ejecta into the hot ambient gas. There also seems to be a characteristic scale for instabilities, but a full modal analysis would be necessary understand its origin.

The Kelvin-Helmholtz (KH) instabilities discussed in the previous section are the main cause of mixing in the wake. If a large wavelength mode grows under pressure equilibrium near the head of the flow, its presence creates a much larger effective collision cross-section for the ambient medium. The ambient medium imparts momentum to these large KH "fingers," and very effectively heats them and advects them downstream above the main wake zone. Occasionally large pieces become completely detached from the wake, and mix even more with the ambient gas. Figure 10 shows growing modes from the initial contact discontinuity that form long fingers that are bent and advected downstream. These colder pieces are

continuously shocked by the ambient gas as they move down the wake.

Although many smaller KH instabilities grow and advect down the flow, the mixing (heating) effects of the largest "fingers" are far greater, since they can dredge up more inner wake material. We can calculate the location in the wake where we expect these large modes to present themselves by multiplying their growth time by the wake flow speed. A KH mode with a wavelength of five parsecs that begins growing near the head of the flow will have an approximate growth time of 7.5×10^4 years. Given an outer wake flow speed of 50 km s^{-1}, this mode should be growing large by about four parsecs downstream, which is consistent with the simulations.

Now that we have established that the location of these modes agrees with predictions, we will examine their considerable influence on the dynamics of the wake. The large blobs and their accompanying vortices move down the wake creating alternating large zones of relatively low and high pressure in the wake. This effect is shown by the pressure map in Figure 11, which also designates three horizontal lines along which pressure profiles were extracted and plotted. These pressure profiles, taken at increasing distance from the symmetry axis, show the dramatic alternating changes in pressure that occur down the wake. The pressure gradient of some of the pressure jumps suggest significant shocks traveling downstream within the wake in conjunction with these fingers. A temperature map of the same region would only show shocks occurring where the large fingers continue to reach out in the ambient gas. The common peaks in these curves seem to suggest characteristic "wavelengths" for the flow on the order of 5 pc. They are spreading apart as they travel downstream because the wake experiences a slight acceleration downstream due to the constant influence of the fast ambient flow. The other main effect of the KH instabilities, regardless of wavelength, comes from the vortices that always form downstream from a growing mode, with the longer modes having larger-scale vortices. These vortices help to create weak shocks as they mix ambient gas into the interior of the wake. This suggests that they play a more important role in heating the stellar ejecta than the initial bow shock and contact discontinuity.

3.3. Cumulative Heating

The discussion of heating mechanisms has been necessarily quite qualitative, but we can obtain an estimate for the cumulative heating by calculating the amount of stellar mass loss that remains cold as a function of distance downstream in the wake. We do this by computing the time-averaged mass flux, $4\pi r^2 \rho v$, through shells of increasing radius for increasing temperature cutoffs. Time-averaging is possible once a quasi-steady state flow has been established. If the mass flux for the colder temperature cutoff bins decreases

signi cantly (i.e. by one or two orders of magnitude) before reaching the edge of the grid, then we will consider that gas as being heated. Both this overall decline in mass ux and the nature of the pro le are important, since the pro le will tell us something of the mechanism primarily responsible for heating that gas. A slow steady decline in the amount of cool material suggests wake vortex and shock heating as the gas is advected downstream. A sharp decline near the head of the ow is due to a strong bow shock and the contact discontinuity heating upon initial contact with the ambient medium.

We calculate these time-averaged mass uxes during a post-processing step that takes grid data for a given time, computes the uxes as a function of radius, and then averages them with every other output between the time when the quasi-steady state ow is established and the end of the simulation. Since the wake ow time is roughly 8 10^5 years, we conservatively use grid outputs for simulation times between 10^6 years and 3 10^6 years, when the simulation ends. For each preset temperature cuto , we step through increasing radii (0:1 25 pc), and compute the combined mass ux for each angular cell i (0 rad) at that radius with an average temperature at or below the current cuto value. If a cell has radial velocity that is negative (i.e. not owing out through the shell), we do not include it in the sum. The outward mass ux for a single cell is given by:

$$\dot{M}(r;) = 2 \; r^2 \quad \max(v_r; 0); \tag{5}$$

where is the angular extent of the outer cell boundary, r = 0:1 pc de nes the inner boundary, and = 0 corresponds to the downstream symmetry axis. Since we sum $\dot{M}(r;)$ for = 0 radians at a given r, the total area of the shell is the full 4 r^2 cm^2. Also, since we only count gas owing outward through these shells (via the $\max(v_r; 0)$ term), the only material included for > =2 is the stellar wind before it reaches the contact discontinuity around r = 0:4 pc. Without this condition, the large negative mass ux e ects of the hot wind for > =2 would obscure all of the other mass ux data in which we are interested. This condition on the cell velocity direction will not include material owing backward due to vortices, but such an e ect should be averaged out over time as the vortices are steadily advected downstream.

The mass ux pro les are shown in Figure 12, where the ve cumulative temperature cuto s are at three increasing fractions of the ambient temperature T_{amb}, at T_{amb}, and for all temperatures (to include shocked gas). Each pro le includes all the gas with a temperature at or below the cuto value. Heating of any gas below T_{amb} is indicated by that pro le falling below the stellar in ow rate of $10^{-7} M_\odot$ yr^{-1}. A steep decline suggests a high heating rate. Because of the de nition of the mass ux $\dot{M}(r)$, if there were no mass loss from a star, $\dot{M}(r) / r^{-2}$, and the "All Temps" line would follow this form exactly. The "All Temps" and

T_{amb} curves would be identical. In the simulations with stellar mass loss, the "All Temps" curve quickly approaches the $\dot{M}(r) \propto r^{-2}$ form as the ambient mass flux exceeds the mass flux from the star.

The mass flux near $r = 0.1$ pc is constant in the stellar wind regime and equal to the stellar mass loss rate $\dot{M}_{star} = 10^{-7} M_\odot$ yr^{-1}. Also, the gap between the "All Temps" and $T_{amb} = 3 \times 10^6$ K line is caused by the gas that is shock heated above the ambient temperature. The profile that includes every temperature rises rapidly at first, suggesting that the initial bow shock and contact discontinuity are the cause. Both this profile and the $T_{amb} = 3 \times 10^6$ K profile continue to rise from this point because the hot ambient flow accounts for the bulk of the mass flux at larger radii as the surface area of the shell increases as r^2. However, it is the fate of the cooler stellar ejecta that is of greatest interest here. If the stellar ejecta did not interact with the hot ambient medium, the stellar ejecta mass flux would be a horizontal line at the contant value of $10^{-7} M_\odot$ yr^{-1} and with a temperature below 10^5 K.

The new information provided by this analysis comes from the behavior of the profiles for cumulative temperatures at and below half the ambient value. Each of these profiles steadily falls below the initial stellar mass loss rate. The mass flux in the lowest temperature bin, $T = 10^5$ K, decreases by three orders of magnitude, suggesting significant heating of the coldest stellar ejecta before it exits the grid. The first result is found in the changing slope of the profiles as they steadily decrease with increasing distance downstream. As mentioned above, such a steady decrease suggests that the gradual vortex mixing and shocking in the wake are responsible for most of the heating rather than the initial bow shock and contact discontinuity. The other important point is that all of the cold gas should eventually be heated, and at a fairly significant rate given the slope of the profiles.

Now that we have discussed the nature of the interaction in the fiducial case without cooling, and detailed our analysis of the heating processes, we will examine simulations that include the effects of radiative cooling on the flow.

4. The Fiducial Simulation with Radiative Cooling

For a system in equilibrium, the cooling of the hot gas as a result of optically thin radiation at X-ray energies is the mechanism opposing the heating effects discussed above. It is precisely this radiation that lead to the initial discovery of the hot gas in elliptical galaxies. We are concerned with how the addition of radiative cooling will effect the dynamics of interaction, and we would expect the key parameter to be the ratio of the cooling time

$_{cool}$ to the time for the wake to be heated and mixed in the absence of heating (we will refer to this as the flow time of the ambient medium, $_{flow;amb}$). These properties of the ambient medium will determine the properties of the cold gas since the wake tries to achieve pressure equilibrium with the surrounding medium. If the cooling time is much longer than the flow time, we would expect very little to change with the addition of the radiative loses. In the discussion of the rest of the simulations, we will examine the nature of the interaction as we change the value of this ratio.

Although the optically thin radiative cooling function $_N$ (T) can be approximated by a power law over limited ranges in temperatures, here we used the full calculated cooling function of Sutherland and Dopita (1993) for a solar metallicity plasma. The cooling function is dominated by collisional metal lines for the temperature range appropriate for our calculations, and so the magnitude of the function varies roughly linearly with metallicity: $_N$ / Z. The actual functional change of $_N$ with metallicity is shown in Sutherland and Dopita (1993), where this roughly linear gradient can be clearly seen.

The key parameter for the simulations with radiative losses is the ratio of the cooling time to the flow time of the ambient gas. Since the cooling rate per unit volume is n^2 $_N$ (T), we can change the cooling strength and thereby the cooling time by adjusting the density n, the temperature T, or the metallicity. The wider range of expected density and its higher power dependence makes density the more attractive parameter to vary, and so we will keep the gas metallicity constant by using only the solar cooling function.

In order to demonstrate that cooling should affect the dynamics of the flow, we can calculate some typical cooling times for the ambient gas in pressure equilibrium with the wake. The instanteous isochoric cooling time for a fully ionized 90% hydrogen, 10% helium (by mass) gas is given by

$$_{cool} = \frac{4}{1} \frac{m_p k_b T}{_N (T)} ; \qquad (6)$$

where is the ratio of specific heats, is the mean molecular weight, m_p is the proton mass, k_b is Boltzmann's constant, and is the mass density. We will always use = 5=3 and = 0:62 in this work. In order to calculate this cooling time for the flow, we use average values of the physical parameters for several regions of the flow. As expected, the cooling time for the undisturbed tenuous hot ambient medium is very long, 10^9 years. However, the cooling times for the post-shock gas in the head and wake of the flow are 6 10^4 years, which are less than the flow time of 3 10^5 years. Therefore, we can expect cooling to be important since these times are of the same order.

There are three obvious differences between the cooling (FDFVC) and non-cooling (FDFV) simulations at the same simulation time (e.g., Figure 13): the bow shock, the Kelvin-Helmholtz instability behavior, and the wake entrainment. The large mode instabilities moving downstream are similar to those in the non-cooling case, and this is shown in Figure 14.

First, the bow shock is stronger and more pronounced than the simulations without cooling. Although the contact discontinuity is in the same location for both cases, the cooling bow shock stands roughly 40% further away from the inner boundary. This is because a large instability finger in the cooling case protrudes an entire parsec further into the ambient material than the in the non-cooling case. Therefore, the ejecta in the cooling case is presenting the ambient gas with an effective interaction cross-section area (R^2) that is about four times larger than the in non-cooling run. This feature is not time-stationary, and these gaseous fingers occur cyclically, developing because a large clockwise-rotating vortex immediately downstream from the head transports material and pushes it out into the flow directly above the head. These fingers are quickly advected downstream and broken up, but this vortex continues to dredge up cold wake gas. The disruption of the cold finger generates small globules that have the distinct appearance of Rayleigh-Taylor instabilities (the familiar mushroom cap shape) on the side finger facing the ambient wind. As the finger is bent to the right, it becomes unstable to Kelvin-Helmholtz instabilities as the cold gas moves parallel with the hot gas that is flowing by (see Figure 15). The appearance of Rayleigh-Taylor instabilities is entirely reasonable because the deceleration of the hot gas as it encounters the cold blob acts as an effective gravitational field in a direction normal to the interface. In the frame of the cold blob, the effective gravitational force is opposite in direction to the movement of the hot gas. Therefore, the classical Rayleigh-Taylor condition for instability is met because a dense gas (the cold blob) lies above a tenuous gas (the hot ambient flow). An illustration of this is shown in the bottom panel of Figure 15. Upon averaging over time, simulations with cooling have a stronger and more pronounced bow shock. A direct consequence is that more momentum is imparted to the ejecta material than in the non-cooling case. Whereas Rayleigh-Taylor instabilities were also identified in the non-cooling case, they are more common in this simulation with cooling.

A second important difference between simulations is that the Kelvin-Helmholtz instabilities are structurally different from those in the non-cooling case. The interaction in the cooling case generally seems more chaotic and unstable than in the non-cooling case. The "fingers" that grow near the head of the flow in the cooling case typically grow more quickly and extend further into the ambient gas than in the non-cooling case. However, if we compare the KH growth time scales for the initial contact discontinuity in both cases, we do not find any significant differences. The cooling case does appear to grow long mode instabilities

while damping out most smaller modes in the wake. Another aspect is that the cooling has damped out the numerical artifact along the upstream axis that is seen in the non-cooling simulations. Both of these effects in the head region can be seen in Figure 16.

The third important difference is that the wake is much more narrow in the cooling case (Figure 13, Figure 17). There is almost no vortex mixing going on in this part of the wake in the cooling case, with the exception of the widely spaced large KH modes that survived from the initial contact region. There are also fewer small scale internal wake shocks generated as these larger modes move downstream.

Finally, there is a significant difference in the amount of mass that cools. We calculate the mass flux in different temperature ranges, as discussed above (Figure 18). The simulations show that most of the heating of the cold stellar ejecta takes place within the first few parsecs of the interaction. The more unstable Richtmyer-Meshkov and Kelvin-Helmholtz growth near the head of the flow leads to a greater momentum transfer and shocking from the ambient medium, and prompt mixing and heating of the gas. In the wake, radiative cooling causes the damping of all but the largest modes that survive the trip downstream. The wake is largely devoid of small scale vortex mixing and shocking. Cold material that survives the initial contact region resides in the very narrow and stable inner wake. The fractional mass flux that remains cold is greater than in the non-cooling simulation, and that fractional amount is increasing as it approaches the outflow boundary of the simulation, presumably due to continued radiative cooling. At the outflow boundary, the fractional amount of gas cooler than 10^5 K is about 10^{-3} for the non-cooling case, but it is 0.15 when radiative cooling is included. Evidently, radiative cooling leads to a significant (but not dominant) fraction of the stellar ejecta remaining cool.

5. The Influence of Ambient Gas Density

The ambient gas density used for the fiducial simulations was chosen to be the typical value in an elliptical galaxy. However, the ambient gas density varies by over an order of magnitude from the center to outer part, so here we investigate the consequences for the evolution of the stellar ejecta when the density is an order of magnitude lower and half an order of magnitude greater than the values used in the fiducial runs.

5.1. High Ambient Density Simulation

We consider the effects of increasing the ambient density to a value that is a reasonable average for the inner 5 kpc region of a typical galaxy (e.g., Vedder, Trester, & Canizares 1988; David, Forman, & Jones 1991), where $n_{amb} = 3.33 \times 10^{-3}$ cm^{-3} (see Table 1; simulation HDFV). Because the stellar wake is in pressure equilibrium with the surrounding medium, increasing the ambient density by 3.33 increases the pressure of the entire system since both the wake and ambient gas temperatures have not changed.

The higher ambient pressure present in this simulation (HDFV) causes the wake to be more narrow than in the fiducial simulation (FDFV). If we assume that the wake temperature is constant for both simulations, the size of the wake should be reduced by a factor of $3.33^{-1/3} \approx 0.7$ when the density is increased by a factor of 3.33 over the fiducial density: $n_{wake} \propto h_{wake}^{-3} \propto p_{system}$; if T = const. In agreement with this approximate scaling relationship, we find that the width of the wake is reduced by roughly 60% compared to the FDFV. The initial contact discontinuity is also closer to the inner boundary because the relatively stronger ram pressure of the ambient gas balances that of the stellar ejecta at a smaller standoff distance r_0. Also, this leads to a less pronounced bow shock. A typical set of grid temperature maps comparing this simulation with the fiducial one are shown in Figure 19.

While the wake may occupy a smaller volume in the high density simulation, it is equally complex as in the fiducial run (Figure 19). There are many large and small mode Kelvin-Helmholtz instabilities in the wake, along with the vortices and shocks that accompany them. This output time shows two large KH fingers and continuing shocks from the ambient gas that survived to large distances downstream. The theoretical KH growth time-scale is $_{KH} \quad 3 \quad 4 \quad 10^{3}$yrs. The flow time $_{flow}$ continues to be two orders of magnitude longer, so we expect the flow to be unstable to the KH instabilities as it clearly the case.

We would expect the heating of the gas to be relatively significant in this simulation despite the reduced collision cross-section of the flow, because the wake is highly KH unstable. The internal mixing and shocking make the wake very complex, more so than in the fiducial simulation. In the downstream direction, the cold stellar mass loss is heated more efficiently than in the fiducial case. The mass fraction of gas cooler than 10^5 K falls to three orders of magnitude below $\dot{M}_{star}$ in roughly half the downstream distance when compared to the fiducial simulation. This is probably due partly to the higher thermal energy content of the ambient medium.

The addition of radiative cooling (simulation HDFVC) has a very strong effect on the flow, especially on the fraction of cool gas in the downstream region. Although the initial

heating occurs more rapidly than in the fiducial case, the increase in the pressure leads to a yet larger increase in the radiative cooling rate. Because the volume cooling rate depends on the square of the density, this simulation should have a cooling rate about ten times higher ($(3.33)^2$) than in the fiducial case. The instantaneous cooling time for a typical region near the wake is $_{cool}$ 2 5 10^4 years, which is about 2 – 6 times less than the fiducial density cooling time, and about half the flow time.

As in the non-radiative case, most of the heating occurs quickly near the head of the flow. Also, the narrowing of the wake is similar to the fiducial case when radiative cooling was introduced (FDFVC). Proceeding downstream, one finds a striking separation between temperature states of the mass loss (Figure 20). Gas cooler than 1.5 10^6 K has cooled below 10^5 K so that it has effectively become cold gas and will not become part of the hot ambient medium. This cooled gas is about one-quarter of the mass lost from the star, and as this value does not change significantly through the last 10 pc of the wake, it appears to be well-defined.

5.2. Low Ambient Density Simulation

In this set of simulations (LDFV and LDFVC), the ambient density is reduced by factor often to $n_{amb} = 10^{-4}$ cm^{-3}, which is representative of the outer regions of an elliptical galaxy. The lower pressure and momentum flux causes the contact discontinuity standoff distance to be about a factor of four larger than in the fiducial run. The ram pressure of the ambient flow has been reduced by an order of magnitude, and the bow shock is correspondingly less effective at heating and transferring momentum to the stellar ejecta. The RM, KH and RT instabilities do not develop rapidly enough to dredge up the inner parts of the expanded wake. Consequently, relatively more heating occurs in the wake region.

For the case without radiative cooling (LDFV), the wake continues to be unstable to KH modes, and RT fingers reach far into the ambient medium. The lower system pressure allows the cold wake material to fill a much larger volume, and it does not appear that there are any KH modes of large enough amplitude to dredge up the inner wake along the axis. So despite surface instabilities and occasional gas parcels that break off from the wake, the central part of the downstream wake is less disturbed. The absence of instabilities large enough to dredge up the inner wake suggest that they do not have enough time to grow because the preferred scale for the instability wavelengths and the growth times have been increased because of the lower density of the simulation. Relative to the fiducial run, a larger fraction (0.11) of the gas cooler than 10^5 K remains when the wake exits the grid. Since the mass fraction at this temperature has not reached an asymptotic value, we expect that it

would continue to decrease had the grid been larger.

When radiative cooling is added (LDFVC), the cooling times are $_{cool}$ 0:3 3 10^6 years, depending on the location in the flow. The geometric mean of the cooling time is about 10 times longer than in the fiducial case and about 10 times longer than the flow time. Consequently, the influence on the dynamics of the flow are not great and the width of the wake is similar in the simulation with and without radiative cooling. Since the relative heating and mixing rate is relatively greater than the radiative cooling rate, we expected more of the stellar mass loss to be converted into the hot ambient medium. However, the mass flux of the gas cooler than 10^5 K is reaching an asymptotic value in the final 5 pc of the flow at 0.2 of the initial mass loss rate (Figure 21). In the last half of the flow, the cooling time in the cool wake is less than the flow time.

6. The Influence of the Star's Velocity

Another important parameter that we consider is the velocity of the star relative to the ambient medium. To study this effect, we consider stellar velocities that are larger and smaller than the fiducial velocity by 125 km s ^{1}. We anticipated that changes in the relative velocity would alter the heating and cooling properties in the sense that the higher velocity simulations would produce hotter shocked gas that has a significantly longer cooling time compared to the fiducial case. The reverse was expected for the lower velocity case, which also has an important difference from the other runs in that the stellar velocity is subsonic compared to the sound speed of the ambient material. Compared to our expectations, the simulations led to some surprising results in that the efficiency of gas heating was different than initial expectations. This is because a fraction of the gas is driven into a wake and the heating of the wake occurs through the excitation KH instabilities of preferred wavelengths, which appear to depend on the flow properties. As the heating rate of the cool wake depends on flow conditions, simulations are the only approach to quantifying the efficiency with which stellar mass loss is converted into hot ambient gas. We simulate the different stellar space velocities by choosing different ambient gas velocities. We continue to use the fiducial values of the ambient density and temperature, as well as same stellar mass loss rate.

6.1. High Stellar Velocity Simulation

In this simulation (FDHV), the Mach number is M 1:8, compared to the value in the fiducial run of 1.3. This leads to a higher ram pressure, a smaller standoff distance for

the contact discontinuity, and a much more oblique bow shock that is closer to the contact discontinuity.

In the non-radiative simulation (FDHV), the KH modes begin to grow into filaments but they become disrupted by the faster shocked ambient material, so the filaments do not grow as large as in the fiducial run. The wake occupies roughly the same cross-section as in the fiducial case and it also contains instabilities, vortices, and internal shocks, but the faster flow prevents the growth of the larger filamentary structures seen in the previous adiabatic wakes. The flow is unstable to Rayleigh-Taylor instabilities, but few structures develop due to the more rapid disruption of the KH filaments. In turn, this prevents large-scale mixing of the inner wake by these modes. Most of the mixing occurs through relatively smaller modes. Another difference in the wake flow near the head is that a secondary shock typically forms roughly four parsecs downstream (Figure 22). Due to the difference in the excitation of KH modes, one would expect a reduction in the cumulative heating rate of this non-cooling fast flow simulation relative to the fiducial case. That expectation is verified by the simulation, but the heating rate is still sufficient to reduced the mass flux of gas cooler than 10^5 K by two orders of magnitude at the point where it exits the grid.

The inclusion of radiative cooling (run FDHVC) makes several dramatic differences in the results, especially in the unstable modes that are excited. Instabilities produce cool filaments near the head of the wake, which are excited and grow more rapidly than in the non-cooling case (Figure 23). Further downstream, the wake is also more unstable and larger modes develop before interacting with the fast surrounding flow (Figure 22). This change appears to be related to the width of the wake, which is narrower due to the loss of thermal energy through radiative losses. In a more slender wake, the size of the most rapidly growing modes has changed, where larger and cooler filaments develop.

As with the other flows that include radiative cooling, most of the heating occurs near the head of the flow. This heating is hastened by the more easily excited instabilities, which undergo mixing and shocks. The greater relative flow velocity of the star leads to slightly more heating within the first few parsecs of the star (relative to the fiducial run), but further down the wake, the higher velocity leads to a larger conversion of cold gas to hot gas (Figure 24). As the gas exits the grid, the remaining fraction of gas below 10^5 K is 0.057 and the value is still decreasing. The higher velocities produce higher temperature gas that cools more slowly, relative to the fiducial case. The effect of a higher stellar velocity is a more efficient conversion of the stellar mass lost into the hot ambient medium by at least a factor of three.

6.2. Low Stellar Velocity Simulation

In this simulation (FDLV), the lower stellar velocity of $v_{amb} = 225$ km s^{-1} results in a subsonic ambient flow with Mach number $M \quad 0.87$ (we will term this simulation the subsonic case, although the ambient gas is still supersonic with respect to the stellar ejecta). The subsonic stellar velocity leads to the absence of a bow shock, which was present in all other simulations (Figure 25). If the mass-losing star were replaced with a solid body, laminar flow around the object would be described by potential flow without any shocks. However, the interaction between the mass loss from the star and the flow around it is not steady in time as the two regions interact to produce a wake and create KH instabilities. These differences relative to the flow around a solid body lead to the development of weak shocks in a flow where the Mach number is close to unity.

In simulations with or without radiative cooling (FDLVC and FDLV), weak shocks develop nearly 10 pc upstream. Kelvin-Helmholtz instabilities grow rapidly, being especially prominent in the several parsec downstream region (Figure 26). In the non-cooling case, this leads to efficient heating so that when the wake exits the simulation, the gas cooler than 10^5 K is about 0.005 of the initial mass flux (Figure 27). When radiative cooling is introduced (FDLVC), there is more active development of KH instabilities that peel off near the head of the flow and in the 10 pc region downstream in the wake (Figure 26). Another difference, also common with other radiative simulations, is that the cool wake is thinner as cool material is more easily compressed. This modifies the axial ratio of the wake, and evidently, the dominant KH growth modes.

An expectation of this lower velocity flow was that the heating would be less effective than in the fiducial run, so more gas would remain cool when radiatives losses were included (run FDLVC). However, calculations fail to support this expectation and the amount of cooled gas is not greater than in the fiducial run and may be slightly less. In the last 10 pc before the gas leaves the grid, the mass flux of cooled gas has reached asyptotic values at 0.14 of the initial mass flux for gas cooler than either 10^5 K or $7.5 \quad 10^5$ K. Even including gas cooler than $1.5 \quad 10^6$ K does not raise the fraction above 0.2 of the initial mass flux. This decrease in the cool mass flux, relative to the fiducial run, is most likely due to the more effective mixing and small-scale shocks that occur in this subsonic simulation.

7. Discussion and Conclusions

We have, for the first time, calculated in detail the interaction between stellar mass loss and the hot interstellar medium in elliptical galaxies using accurate two-dimensional

numerical hydrodynamics simulations. The ultimate fate of the stellar ejecta has significant implications for the standard theory of the interstellar medium in elliptical galaxies, because this mass loss is the primary origin of the 1 keV X-ray gas in these galaxies. We examined whether the optically thin radiative cooling of the gas will prevent some stellar ejecta from being shock heated to the local velocity dispersion temperature and entering the ambient flow. Simple calculations suggest that the fraction of stellar mass loss that remains cool might depend strongly the density of the surrounding and the velocity of the star relative to the hot ambient interstellar medium (Table 2). For the simulations of this process, we calculated a reference (fiducial) case against which changes in density and stellar velocity were compared. Different ambient densities are naturally encountered in early-type galaxies, where the density is considerably larger in the inner part compared to the outer region. Variations in the stellar velocity occur in the orbit of every star. For each set of initial conditions, two simulations were calculated, one with and one without radiative losses. The gas exiting the grid may have a mean temperature larger or smaller than the initial ambient temperature. It will have either greater or less entropy than the surroundings, and in pressure equilibrium with its surroundings, will be positively bouyant and rise outward in the galaxy, or flow inward. We will not consider this complication here, as it occurs on a timescale longer than the flow time of the calculations.

For the runs where the stellar velocity was supersonic, it had a Mach number of $M = 1.3 - 1.8$, and this led to a bow shock in the ambient medium at about the theoretically expected standoff distance, 1 pc upstream. Whereas the stellar mass loss is also shocked, this is not the event that is the primary heating mechanism for the cool gas, although most of the heating occurs in the region near the star, within 3 pc downstream. The initial interaction of the streaming ambient ISM with the stellar ejecta imparts momentum to the ejecta that begins to drive it downstream. The flow past the cold ejecta is Kelvin-Helmholtz unstable, and fingers of material are drawn out perpendicular to the intial flow axis. This greatly increases the cross section of the stellar ejecta, leading to heating by shocks that are driven into the cooler material by the rapidly flowing ambient medium. The other important mechanism is the mixing between the fast-flowing hot gas and the stellar ejecta, which occurs through the presence of vortices and the development of Rayleigh-Taylor instabilities. These instabilities and the related heating occur further down the wake as well, and in the absence of radiative cooling, nearly all of the gas has been heated and will eventually become part of hot ambient medium. We constructed our fixed grid so that nearly all of the important processes occur before the flow exits the grid (25 pc downstream from the star). The timescales proved to be longer for the low-density run (LDFV, LDFVC), where the cool material is still decreasing as the gas exits the grid.

When radiative cooling is included, and when the cooling time of the gas is small enough

to be dynamically important, there is an increase in the upstream mixing and heating of the ejecta by instabilities, but any material that is not promptly heated near the head of the interaction condensed into cold blobs or flowed onto the central wake. There continues to be instabilities between the cold wake and the hotter and faster flow, which produces a net heating rate. There is also a radiative cooling rate associated with the wake and if the evolution of the wake depends strongly upon whether this is larger or smaller than the heating process. Also, the heating due to shocks and mixing decreases with downstream distance, so the two can eventually balance or the cool component in the wake can even grow if it cools the hotter material as it mixes in. This appears to be the case in the fiducial run, where 15% of the gas is cold ($< 10^5$ K) when it exits the grid. However, as the flow approaches the last 10 pc of the grid, the mass flux fraction below 10^5 K is rising as the fraction of gas in the $10^5 - 1.5 \times 10^6$ K range is falling. Most of the gas in the $10^5 - 1.5 \times 10^6$ K range appears to be heated and join the hot ambient medium, but some fraction grows onto the wake. We estimate that about 20% of the gas might remain cold if the simulation could be extended to larger radii.

We expected the density of the ambient medium to be crucial in determining the amount of stellar ejecta that remained cool. This is because the wake material tries to approach pressure equilibrium with the hot ambient flow. Consequently, a higher ambient density gives rise to an increased density in the cooler wake, and at a given temperature, the radiative cooling rate increases as the square of the density. However, the higher density simulation shows that while a high density (pressure) entrains the wake more, it also magnifies the strength of the Kelvin-Helmholtz instabilities as they mix and shock the inner wake material. This leads to an increased heating rate that partly offsets the increased cooling rate. The simulations show that there is an increase in the amount of stellar ejecta that remains cool, but that increase is rather modest. Where the flow exits the grid, 25% of the initial stellar mass loss is cold ($< 10^5$K), 5 – 10% more than in the fiducial run. Even in the low-density run, there appears to be some cold material remaining, although those mass flux values have not reached stable asymptotic limits and appear to be decreasing. We regard the nominal mass flux for the cold gas of 19% as an upper limit and not a reliable value.

Variation of the stellar velocity naturally changes the temperature of the shocked material, where higher stellar velocities produce gas at a higher temperature. For the higher velocity case, we expected greater heating and shorter growth times for the KH instability, as the instability is inversely proportional to the relative flow velocity. These combined effects led to significantly less cool gas remaining in the wake, where 5.7% of the initial stellar mass loss remained cold ($< 10^5$K) as it exited the grid, but this fractional amount is still slowly declining. Compared to the fiducial case, faster moving stars have their mass loss more efficiently heated to the ambient gas temperature.

The opposite expectation, that more gas will remain cool for lower velocity stars, was not supported by simulations. The lower stellar velocity, 225 km s^{-1}, has a Mach number slightly below unity, so a bow shock is not produced. However, the interaction with the stellar mass loss leads to time-dependent structures that produce shocks in the stellar mass loss as well as in the ambient hot gas. For the runs without radiative cooling, there is more rapid heating of the stellar mass loss through shocks and mixing, compared to the fiducial case. For the runs with radiative cooling, most of the heating occurs even more rapidly within 2 pc of the star, but for distances further downstream, radiative cooling exceeds heating for the remaining cool gas ($< 10^5$K). The final amount of cool gas exiting the grid is similar to, but slightly less than the amount in the fiducial run.

One of the surprises of the simulations is that there are dominant modes in the growth of Kelvin-Helmholtz instabilities. The classical calculation has no preferred wavelength, so the smallest modes grow first, as they have the fastest growth rate. However, that calculation assumes the the two fluids have an infinite size and issues such as radiative cooling are not present. In these calculations, the wake that is produced has a characteristic size and for the radiative flows, there is a characteristic cooling time as well. Hardee & Stone (1997) studied the related situation of radiatively cooling jets and found the growth of preferred modes arising from Kelvin-Helmholtz instabilities (Xu et al. 2000). The preferred growth modes found in our simulations may arise from the same physical basis and we will analyze this aspect in an upcoming work.

There are a number of shortcomings in these simulations and various issues that still need to be addressed. One improvement would be to employ a full three-dimensional geometry. This will eliminate the numerical problems that accompany an axisymmetric geometry. Also, the number of possible instability modes is likely to increase in three dimensions, which would affect the mixing of the wake and the amount of gas that would ultimately remain cool (Bodo et al. 1998), although experience has show that it can be difficult predicting the outcome of moving to three-dimensional calculations with any accuracy. Another improvement would be to extend the grid and better resolve regions of enhanced activity through subgridding.

A third possible improvement is the inclusion of magnetic fields. The inner regions of elliptical galaxies have small magnetic field strengths of $B \sim 1$ G (Mathews & Brighenti 1997), and the standard argument against considering magnetic fields in simulations such as ours is that the kinetic energy density of the gas is several orders of magnitudes larger than the magnetic energy density: $U_{KE}/U_B \sim 10^3$. Most studies of magnetic fields in elliptical galaxies concern possible dynamo mechanisms to create the stronger ~ 50 G fields seen in galactic halos (Lesch & Bender 1990; Moss & Shukurov 1996; Mathews & Brighenti 1997).

However, work by Jones et al. (1997) on the role of very weak magnetic fields in the evolution of vortices generated by Kelvin-Helmholtz instabilities indicates that the dissipative influence of magnetic fields on such instabilities should not be ignored. It is clear that the twisting and compression of fields in the stellar wind can make magnetic fields important. The general effect of magnetic fields would be to stabilize the wake against instabilities, thereby reducing the degree of heating and mixing. The strength and topology of magnetic fields will help determine the importance of conduction and viscosity. Given the complicated mixing flows, the downstream magnetic field is likely to be tangled, which supresses conduction.

Another parameter that should be investigated is the metallicity of the mass lost from the star. The metallicity of the gas is important for the radiative cooling in this temperature range, as most of the cooling is due to atomic lines. Higher metallicity leads to shorter cooling times and presumably a greater fraction of the stellar mass lost remains cool. This would lead to lower metallicity gas preferentially being added to the hot medium.

Provided that more sophisticated calculations do not change the basic result of this work, our simulations imply that there would be small amounts of cool gas distributed around a galaxy. There would be a preference for such material to be more common in regions of higher ambient gas density, which occurs in the inner parts of the galaxy. For a given ambient density, the cooled gas would preferentially originate from stars with elevated metallicities and that are not on the high velocity part of the Maxwellian distribution. One implication is that there would be cool gas available for photoionization by the UV-rising branch of the spectral energy distribution of early-type galaxies. Warm ionized gas is frequently detected from early-type galaxies, and in many cases, the spatial distribution is similar to that of the stars, consistent with the predictions from our simulations (Caon et al. 2000). Although the distribution of the optical emission line gas is consistent with our expectations, the velocity structure is often different than expected. We would predict that the cooled gas should have the same rotational velocity axis, yet some fraction of the galaxies show the gas to be counter-rotating when compared to the stars. At least in those galaxies, an external origin for the gas seems more likely (Caon et al. 2000).

Our calculations follow the wakes during their initial heating and cooling stages, but the cooled wakes lack the buoyancy of the hotter gas, so they will eventually sink inward. The interaction of the wakes with their surroundings during this inflow stage is beyond the scope of our calculations. The material may ultimately be heated and mixed into the ambient medium, or act as nucleation sites for further cooling. Gas and dust are seen in the inner parts of early-type galaxies and this could be the end result of cooled wake material that has flowed inward (Temi et al. 2007).

A complementary process is that there is a fraction of the hot ambient gas that is heated

above its initial value. This hotter gas will be buoyant and rise outward in the galaxy. This heating of the ambient gas may be one of the sources that leads to the ambient gas being above the velocity dispersion temperature of the galaxy.

There is a bias in that the mass loss from higher velocity stars is more readily heated. As a consequence, the temperature of the hot ambient medium would be greater than the velocity dispersion temperature, even in the absence of any supernova heating. Extrapolating from our results, this would cause the ambient temperature to lie 10% above the velocity dispersion temperature.

Finally, there are two modes of mass loss that were not considered here: planetary nebulae and supernovae. A planetary nebulae is an event that is more discrete in time, so it presents different challenges to numerical modeling. We have worked on this issue and it will be presented in a future work. We have no plans to study numerically the evolution of supernovae in the hot environment found in an early-type galaxy.

JRP would like to give special thanks to Philip Hughes and Hal Marshall for their valuable advice and comments during code development, simulations, and on the content of my PhD Thesis. Also, thanks are due to Gus Evrard and Douglas Richstone for serving on JRP's thesis committee and for providing timely support and advice. Financial support is gratefully acknowledged and was provided to JRP through a Department of Energy Computational Science Graduate Fellowship and to JNB through a Long Term Space Astrophysics Grant from NASA.

REFERENCES

Athey, A.E. 2003, Ph.D. Thesis, University of Michigan.

Baranov, V.B., Krasnobaev, K.V., & Kulikovskii, A.G. 1971, Sov. Phys. Dokl., 15, 791

Blondin, J.M., & Lufkin, E.A. 1993, ApJS, 88, 589

Blondin, J.M. 1998, private communication

Bodo, G., Rossi, P., Massaglia, S., Ferrari, A., Malagoli, A., & Rosner, R. 1998, A&A, 333, 1117

Body, K.M. 1992, Univ. of Michigan Ph.D. thesis

Brighenti, F., & Mathews, W.G. 2005, ApJ, 630, 864

Brown, B.A., & Bregman, J.N. 1998, ApJ, 495, L75

Canizares, C.R., Fabbiano, G., & Trinchieri, G. 1987, ApJ, 312, 503

Caon, N., Macchetto, D., & Pastoriza, M. 2000, ApJS, 127, 39

Colella, P., & Woodward, P.R. 1984, Journal of Computational Physics, 54, 174

David, L.P., Forman, W., & Jones, C. 1991, ApJ, 369, 121

David, L.P., Jones, C., Forman, W., Vargas, I.M., & Nulsen, P. 2006, ApJ, 653, 207

Dinge, D. 1997, ApJ, 479, 792

Dyson, J.E. 1975, Ap&SS, 35, 299

Frank, A., Balick, B., & Riley, J. 1990, AJ, 100, 1903

Fujita, Y., Fukumoto, J., & Okoshi, K. 1996, ApJ, 470, 762

Fujita, Y., Fukumoto, J., & Okoshi, K. 1997, ApJ, 488, 585

Hardee, P.E., & Stone, J.M. 1997, ApJ, 483, 121

Humphrey, P.J., & Buote, D.A. 2006, ApJ, 639, 136

Irwin, J., Sivakoff, G.R., Sarazin, C.L., Ji, J., Bregman, J.N., & Mathews, W.G. 2006, American Astronomical Society Meeting Abstracts, 209, # 04.14

Jones, T.W., Gaalaas, J.B., Ryu, D., & Frank, A. 1997, ApJ, 482, 230

Lamb, H., Sir 1945, Hydrodynamics (6th ed., New York: Dover), 373

Lesch, H., & Bender, R. 1990, A&A, 233, 417

Mathews, W.G. 1990, ApJ, 354, 468

Mathews, W.G., & Brighenti, F. 1997, ApJ, 488, 595

Mathews, W.G., & Brighenti, F. 2003, ARA&A, 41, 191

Matsumoto, H., Koyama, K., Awaki, H., Tsuru, T., Loewenstein, M., & Matsushita, K. 1997, ApJ, 482, 133

Moss, D., & Shukurov, A. 1996, MNRAS, 279, 229

Parriott, J.R. 1998, Ph.D. Thesis, University of Michigan.

Riemers, D. 1975, in Problems in Stellar Atmospheres and Envelopes, eds. B. Baschek, W. H. Kegel, & G. Traving (Berlin: Springer Verlag), 229

Renzini, A., Ciotti, L., D'Ercole, A., & Pellegrini, S. 1993, ApJ, 419, 52

Sutherland, R. S., & Dopita, M. A. 1993, ApJS, 88, 253

Temi, P., Brighenti, F., & Mathews, W. G. 2007, ApJ, 660, 1215

Trager, S. C., Faber, S. M., Worthey, G., & Gonzalez, J. J. 2000, AJ, 120, 165

Turatto, M., Cappellaro, E., & Benetti, S. 1994, AJ, 108, 202

Vedder, P. W., Trester, J. J., & Canizares, C. R. 1988, ApJ, 332, 725

Wilkin, F. P. 1996, ApJ, 459, L31

Xu, J., Hardee, P. E., & Stone, J. M. 2000, ApJ, 543, 161

Table 1. Simulation Input Parameters

Model	Ambient Medium n (10^{-3} cm^{-3})	Ambient Medium v (km s^{-1})	Ambient Medium T (10^6 K)	Stellar Ejecta n (10^{-3} cm^{-3})	Stellar Ejecta v (km s^{-1})	Stellar Ejecta T (10^6 K)
FDFV	1	350	3	1	35	1
HDFV	3.33	350	3	1	35	1
LDFV	0.1	350	3	1	35	1
FDHV	1	475	3	1	35	1
FDLV	1	225	3	1	35	1

Note. — (F)iducial, (H)igh, (L)ow, (D)ensity, (V)elocity

Table 2. Fraction of Cold and Ward Mass Ejecta Remaining

Model	Non-radiative T 10^5 K	Non-radiative T 7.5 10^5 K	Radiative T 10^5 K	Radiative T 7.5 10^5 K
FDFV	1.4 10^{-3}	0.40	0.15	0.19
HDFV	0	0.18	0.25	0.26
LDFV	0.11	0.59	0.19	0.58
FDHV	1.1 10^{-2}	0.62	5.7 10^{-2}	0.16
FDLV	4.6 10^{-3}	0.10	0.14	0.14

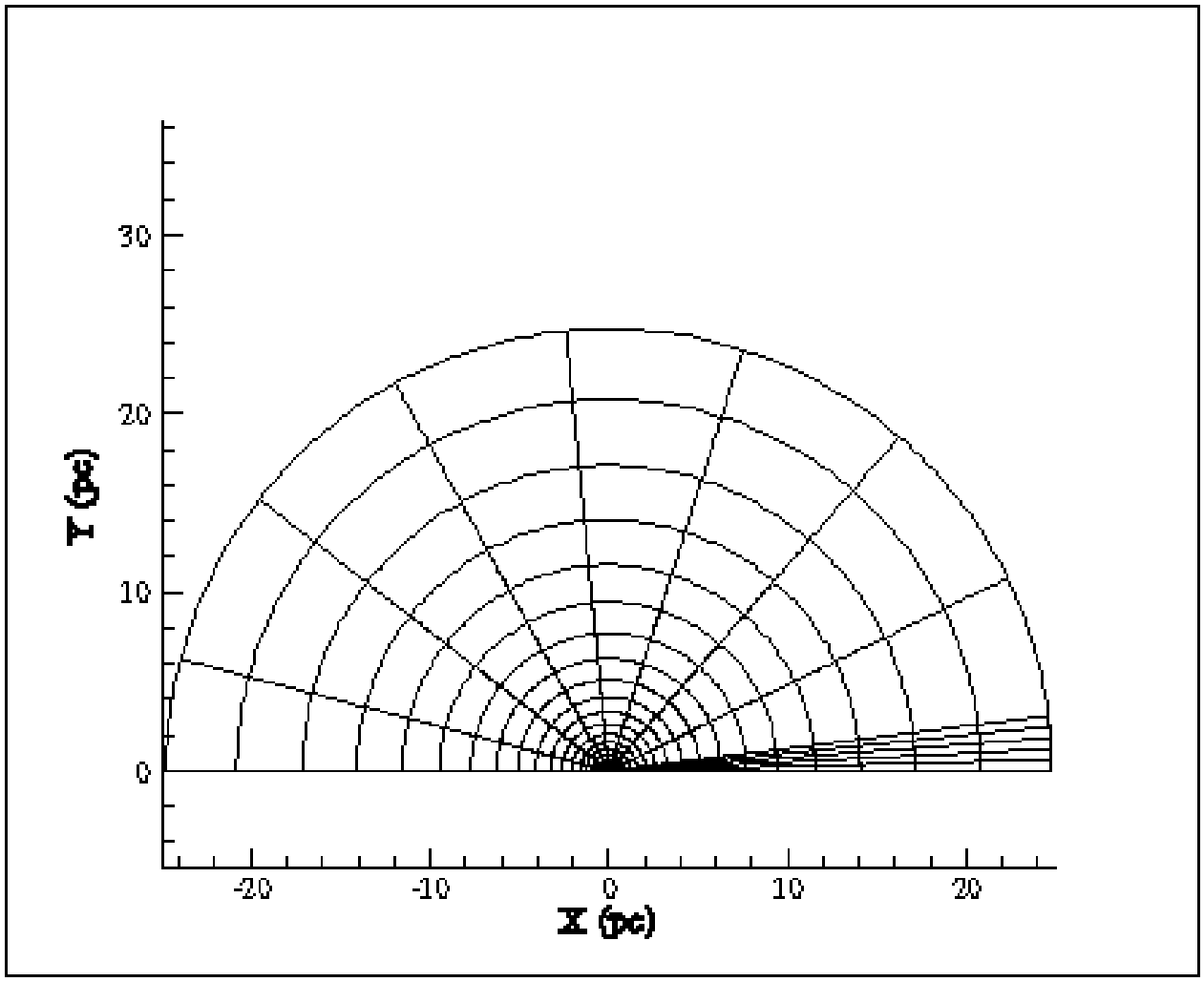

Fig. 1.— The 2-D axisymmetric spherical polar grid mesh used for every simulation in this work. The resolution, determined by the spacing of the radial and angular cells, is highest near the center and in the downstream wake region. For clarity, this figure only shows the radial and angular cells in 20-cell increments (there are 360 radial cells and 240 angular cells). The polar axis is horizontal in this figure; further details are given in the text.

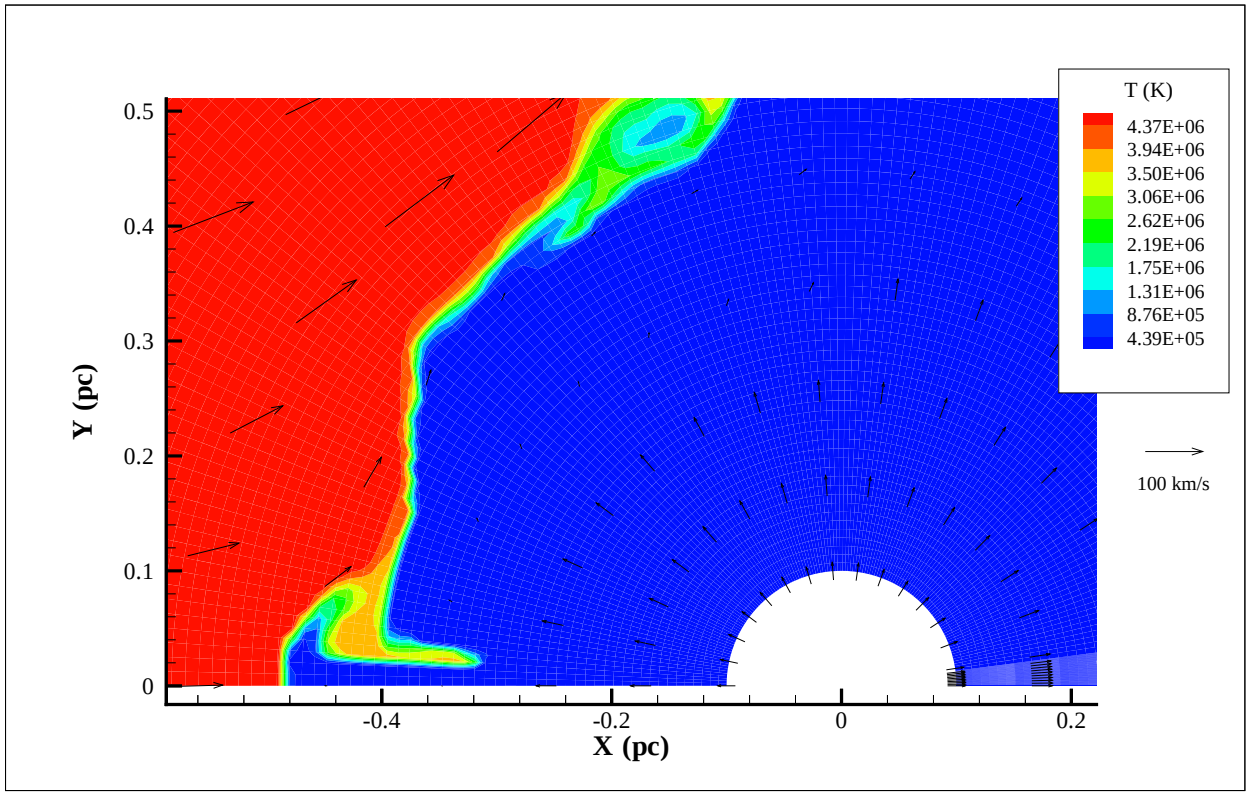

Fig. 2.— Example of upstream extension of gas along symmetry axis, shown with the temperature map. This small amount of material is found 0.04 parsecs further upstream than the contact discontinuity for the stellar wind.

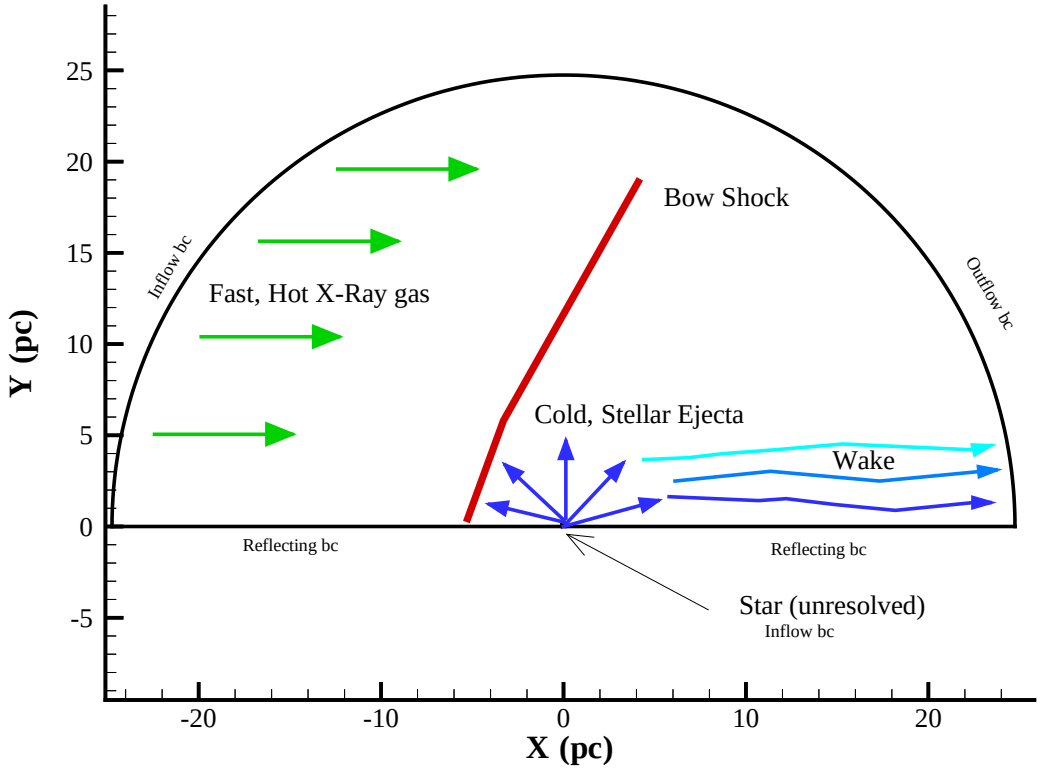

Fig. 3.— Cartoon of the simulation. The hot ambient medium flows from left to right across the grid past the fixed star, encounters the cold stellar ejecta and a bow shock is formed. Momentum transfer pushes the ejecta into a wake behind the star that is full of internal shocks and vortices. The contact surface between the ejecta and ambient medium is unstable to Kelvin-Helmholtz instabilities. The grid boundary conditions are also shown.

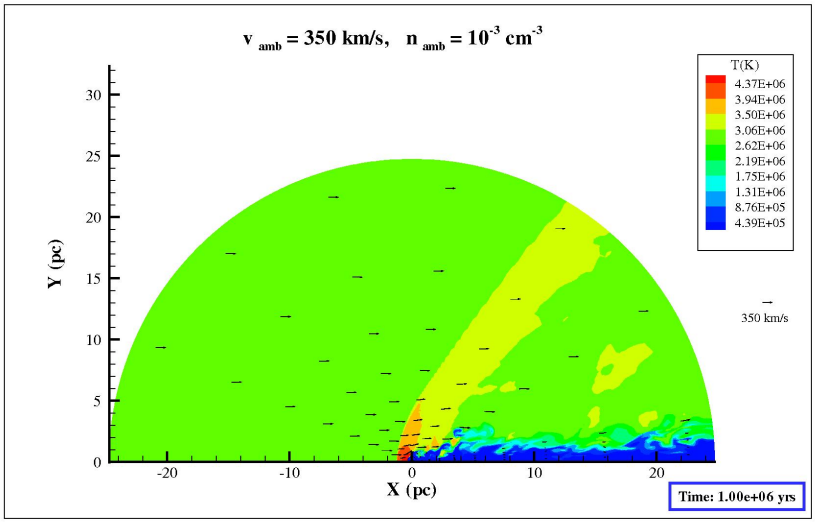

Fig. 4.— Temperature map of the fully developed quasi-steady state flow in pressure equilibrium with the surrounding medium at a simulation time of 10^6 years. This is the fiducial run without cooling, FDFV. The bow shock and unstable wake are fully formed. Numerous Kelvin-Helmholtz instabilities are formed along the contact surface of the wake. The velocity

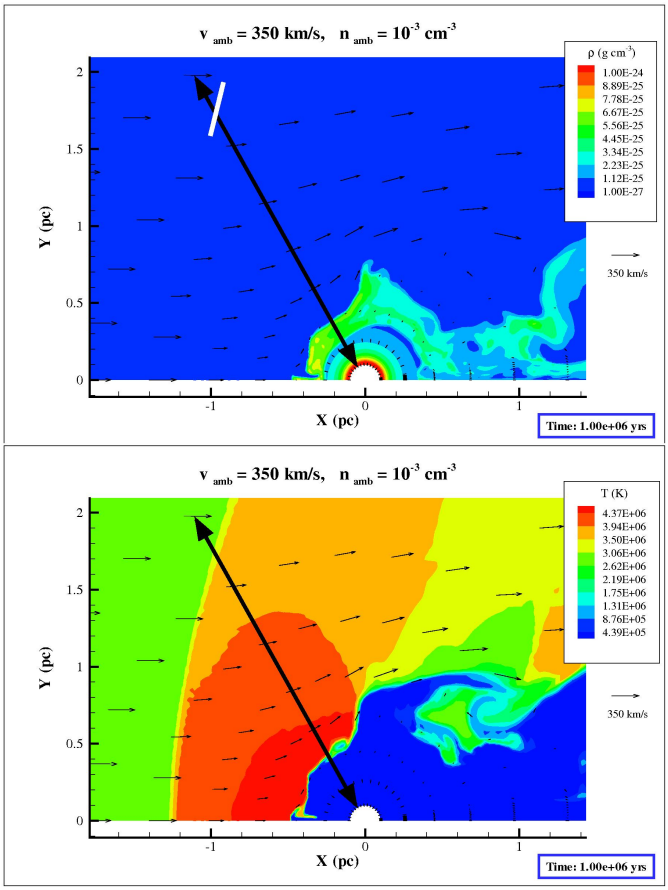

Fig. 5.— Temperature maps of the leading edge collision between the stellar wind and the ambient flow, with density shown in the top panel, and temperature in the bottom panel (for the fiducial run FDFV). The black arrow shows the line where data were extracted to make the plots in Figure 7. The maps show the bow shock and contact discontinuity, as well as a developed KH instability that is peeling off to produce a larger effective area for the ambient medium to shock heat. The small leakage along the upstream reflecting symmetry axis that is caused by numerical error is also shown. The white line on the density map marks the location of the bow shock. The velocity field is shown by the smaller black arrows.

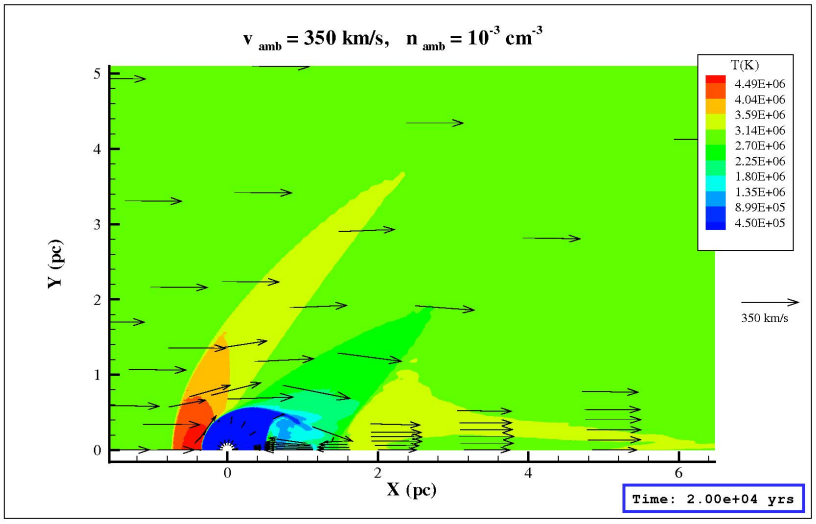

Fig. 6.— The temperature map showing the initial bow shock formation in the M = 1.4 flow, due to the inflow from the inner boundary (run FDFV). A large eddy formed on the immediate downstream side of the outflow can also be seen. The velocity field is shown by the arrows, with the magnitude set by the reference vector at the right.

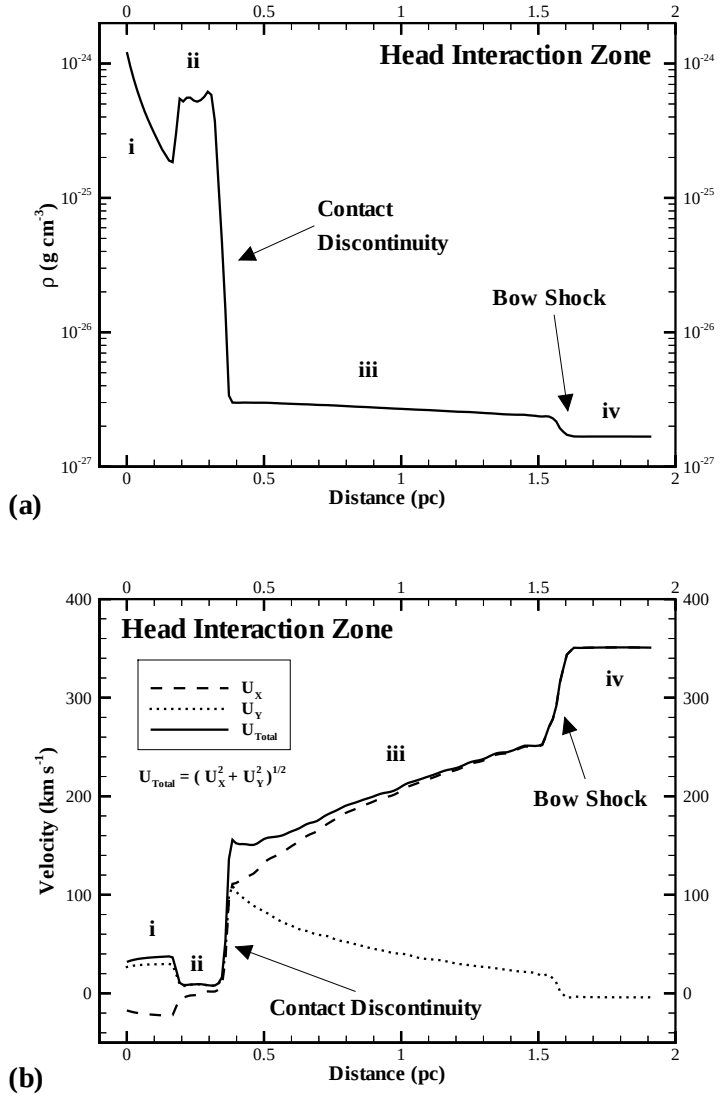

Fig. 7.— Selected profiles of the leading shock zone from data taken along the line designated in Figures 5, run FDFV. (a) Mass density profile, with the contact discontinuity and bow shock designated. The abscissa gives the distance in parsecs along the line, beginning at the inner grid boundary. Region specifications: i) the undisturbed stellar wind, r^{-2} adiabatic expansion; ii) post-shock region from the contact discontinuity shock; iii) post-shock zone from the bow shock; iv) unaffected $M = 1.4$ hot ambient medium. (b) Velocity profiles, with the same specifications as the mass density profile. The X-direction, Y-direction, and combined velocities are shown. The extraction line was chosen to cross the contact discontinuity at a place where the "ambient" and wind velocity vectors were aligned (see text), so U_{Total} was used for the velocities in the KH growth time calculations.

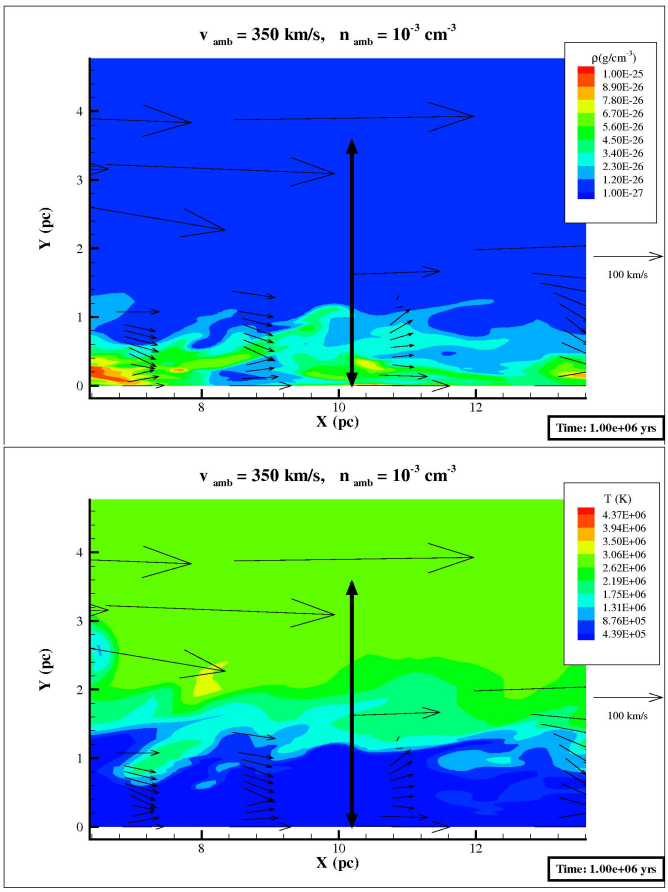

Fig. 8.— Temperature maps of a typical wake region, with density shown in the top panel, and temperature in the bottom panel (run FDFV). The vertical black arrow shows the line where data were extracted to make the plots in Figure 9. The discontinuity interface here is a much wider shear layer, but KH instabilities still grow. The maps show a very unstable and complex wake with numerous KH "fingers" and accompanying vortices being advected along the wake. The velocity field, shown by the smaller black arrows, shows the mixing taking place, as alternating areas of high and low density (pressure) between KH eddys.

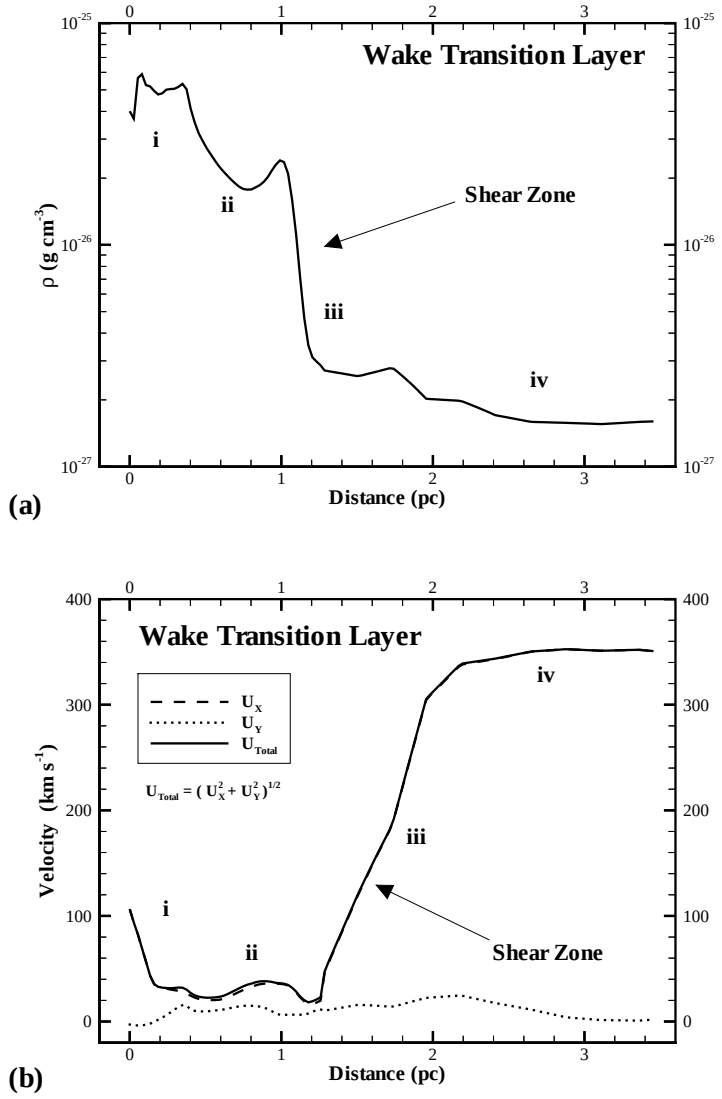

Fig. 9.| Selected profiles of the leading shock zone from data taken along the line designated in Figure 8 (run FDFV). (a) Mass density profile, with the wide shear zone designated. The abscissa gives the vertical distance in parsecs, beginning at the bottom edge of the grid. Region specifications: i) more dense and fast wake material, which could be partially numerical in origin; ii) the main wake area filled with instabilities and vortices; iii) the wide mixing shear zone between the wake and hot medium; iv) relatively unaffected ambient material, with the exception of an occasional disruption by large advected KH "finger."

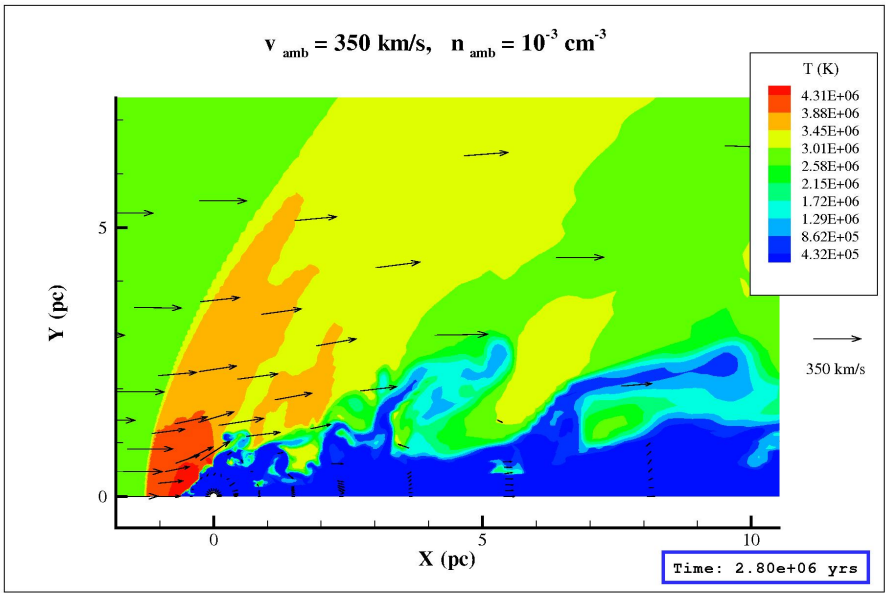

Fig. 10.— Temperature map of growing KH "fingers" that are advected downstream, and continuously shocked and bent by the ambient gas (run FDFV). The largest modes can reach quite far into the surrounding gas, and even become detached from the wake altogether.

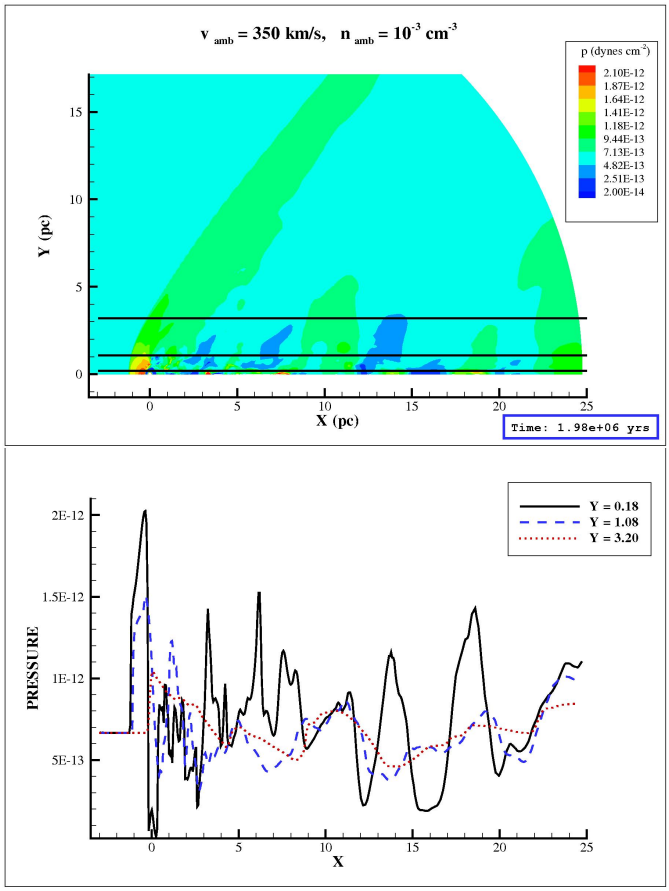

Fig. 11.— Pressure map and profiles for the entire wake, with the horizontal black lines on the map designating the locations where data were extracted to make the profiles in the lower panel (run FDFV). These profiles were taken at increasing distance away from the symmetry axis ($Y = 0.18; 1.08; 3.20$ pc), and show the complex nature of the wake compared to the region dominated by the ambient flow. The common peaks seem to suggest characteristic "wavelengths" for the flow on the order of 5 pc. The dip in the $Y = 0.18$ profile occurs because it passes through the pure stellar wind region near the inner inflow boundary.

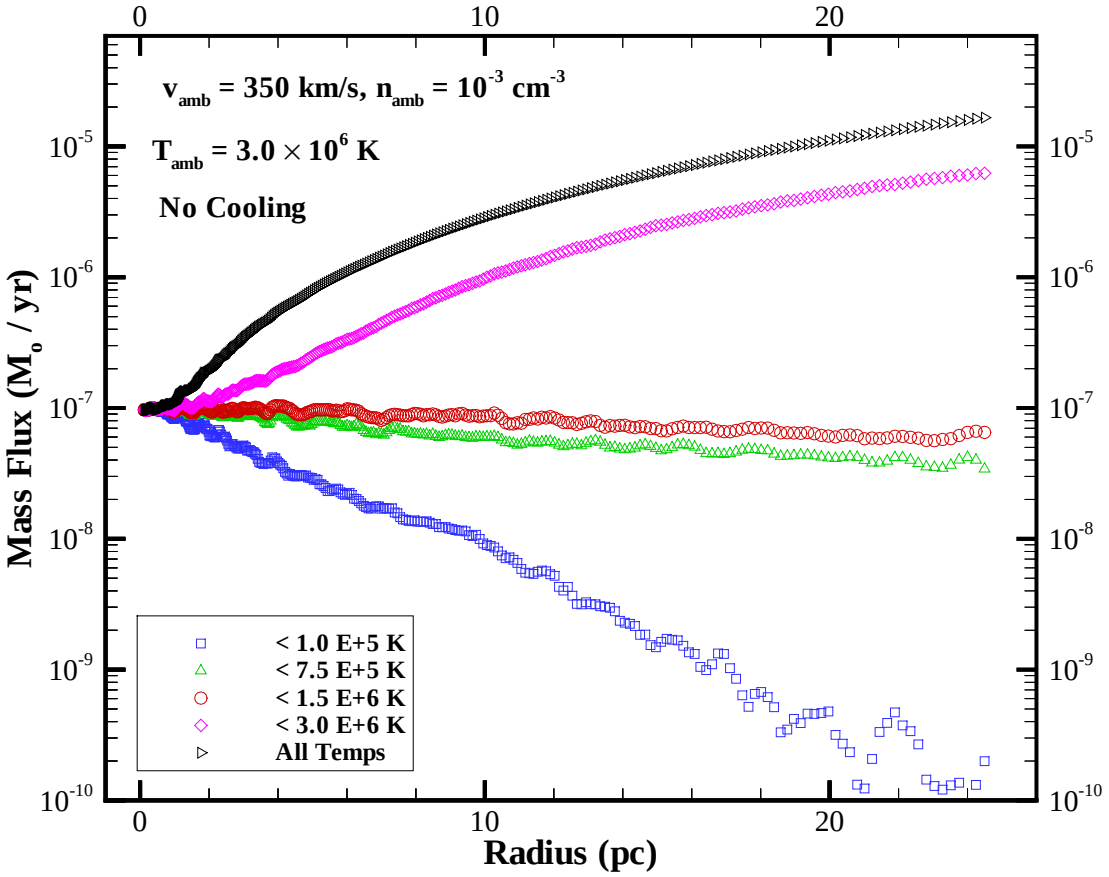

Fig. 12.— Mass fluxes for the fiducial simulation without cooling (run FDFV), as a function of radius. The difference between the "All Temps" line and the T_{amb} = 3 10^6 K line represents gas shock heated to above the ambient temperature. As expected, the value near the inner boundary equals the stellar mass loss rate, which is constant for the pure wind region corresponding to zone (i) in Figure 5. All of the profiles for temperature cutoffs at or below T_{amb}=2 experience a steadily decreasing mass flux, with the 10^5 K profile steadily dropping to a value roughly three orders of magnitude lower than $\dot{M}_{star}$. These profiles suggest constant heating of the cold gas as it flows downstream.

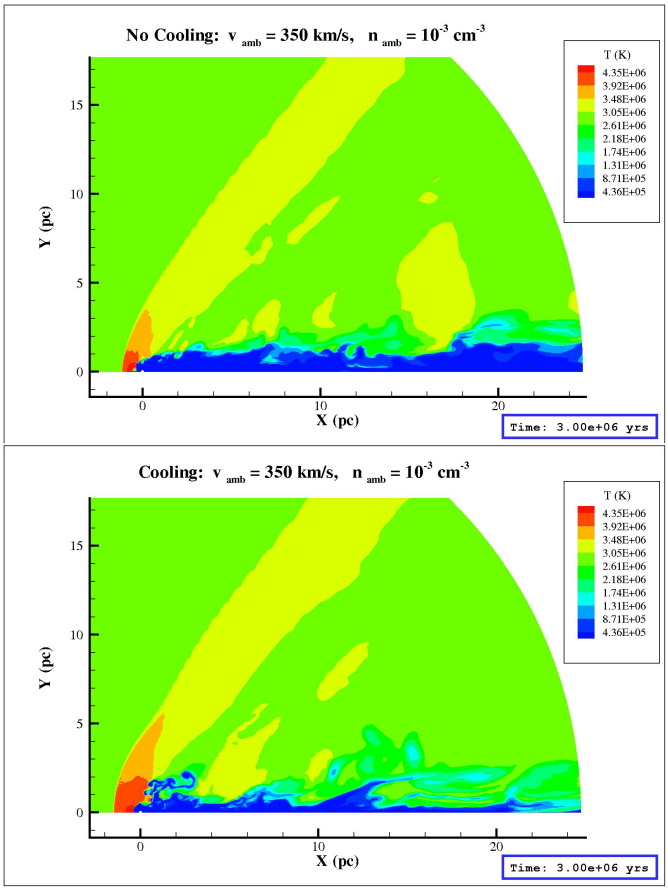

Fig. 13.— Typical maps for cooling vs non-cooling fiducial runs taken at a simulation time of 3×10^6 years. The simulation without cooling is in the top panel (run FDFV), and the run with the addition of radiative losses is in the bottom panel (run FDFVC). These temperature maps, using the same scales, show significant differences in the bow shock, in KH instability behavior, and in the concentration of the wake.

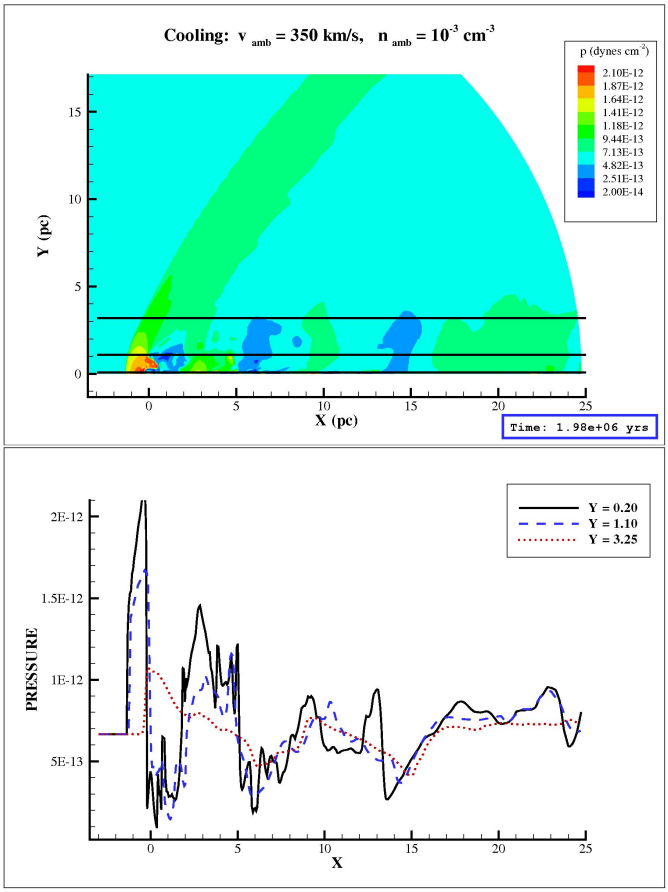

Fig. 14.— Pressure map and profiles for the entire wake, with the black lines on the map designating the locations where data were extracted to make the profiles in the lower panel (run FDFVC). As for the non-cooling case, these profiles were taken at increasing distance away from the symmetry axis (Y = 0.20; 1.10; 3.25 pc), and while the wake is less complex in this case, there are still large KH modes moving downstream that cause the pressure fluctuations.

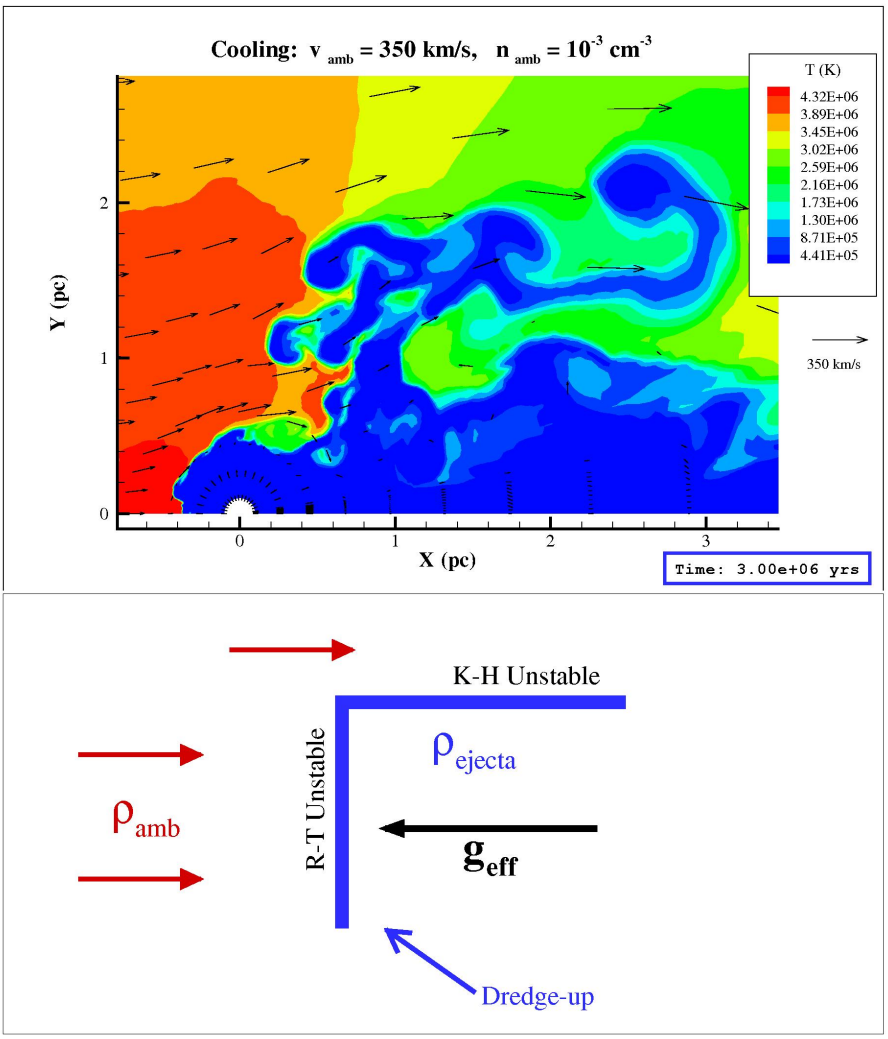

Fig. 15.— Rayleigh-Taylor and Kelvin-Helmholtz instabilities are both seen forming as this cold blob is dredged up and thrust into the ambient flow (run FDFVC). The RT occurs because an effective gravitational force is set up in the opposite direction of the flow, and the KH occurs because the ambient flow is slipping past the cold blob. The bottom panel

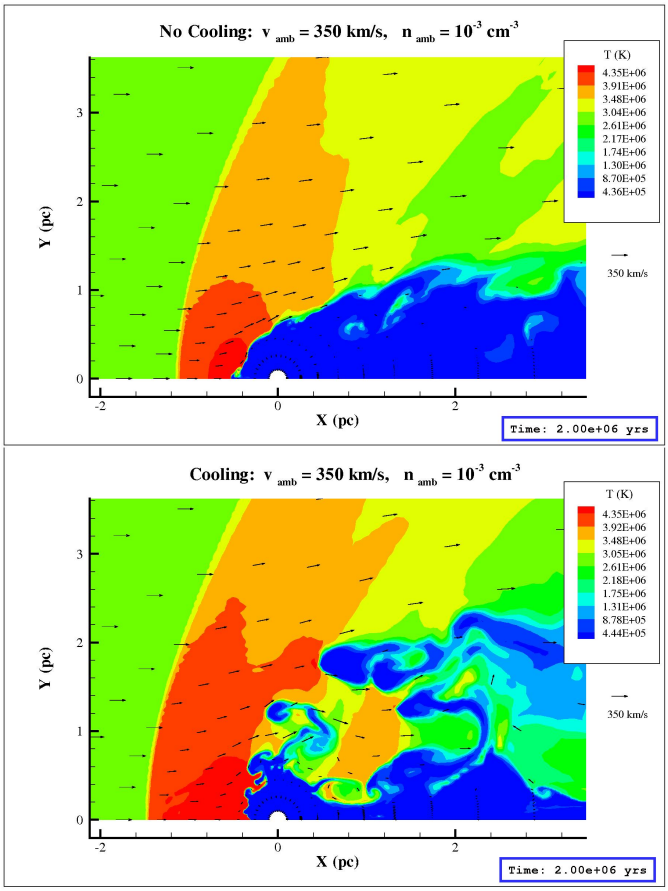

Fig. 16.— Closeup maps showing the difference in KH instability growth at a simulation time of 2×10^6 years (run FDFVC). The difference in the general stability of the flow near the head of the interaction can be clearly seen in these temperature maps. Cooling is shown in the bottom panel, with non-cooling in the top panel. The velocity field is shown by the black arrows.

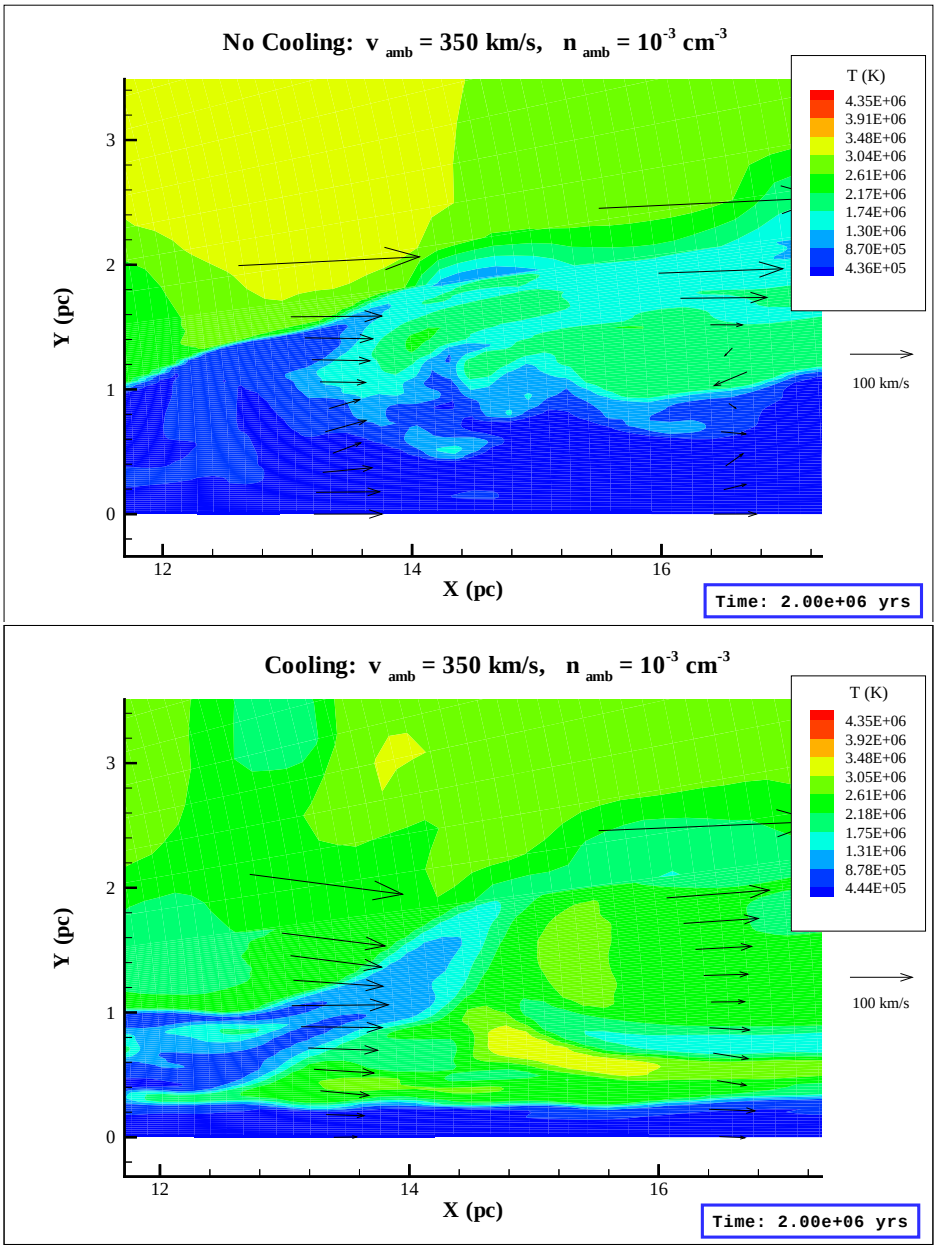

Fig. 17.— Closeup temperature maps showing the difference in wake entrainment at a simulation time of 2×10^6 years. The wake in the cooling simulation (bottom panel; run FDFVC) is much more narrow and entrained than in the more unstable non-cooling case (top panel; run FDFV). The velocity field is shown by the black arrows.

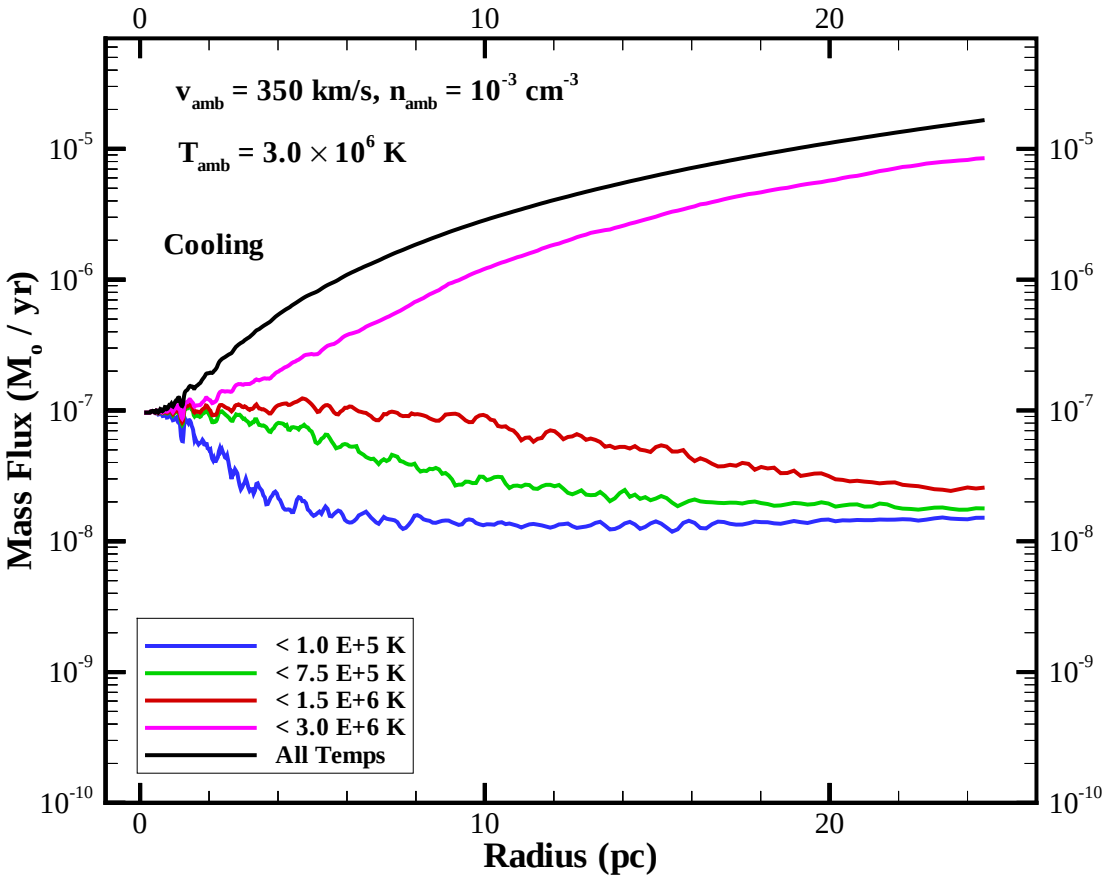

Fig. 18.— Mass fluxes for the fiducial simulation with cooling (run FDFVC), as a function of radius. The data are arranged as in Figure 12. The cold gas is promptly heated near the head of the flow in the first five parsecs, then remains at this level for the rest of the flow. The cold gas fraction of the wake grows slightly between 10 and 20 pc. These profiles suggest heating of the cold gas by the bow shock and instabilities before it flows downstream. Once the cold gas settles into the more narrow wake, further net heating is effectively supressed by the radiative cooling.

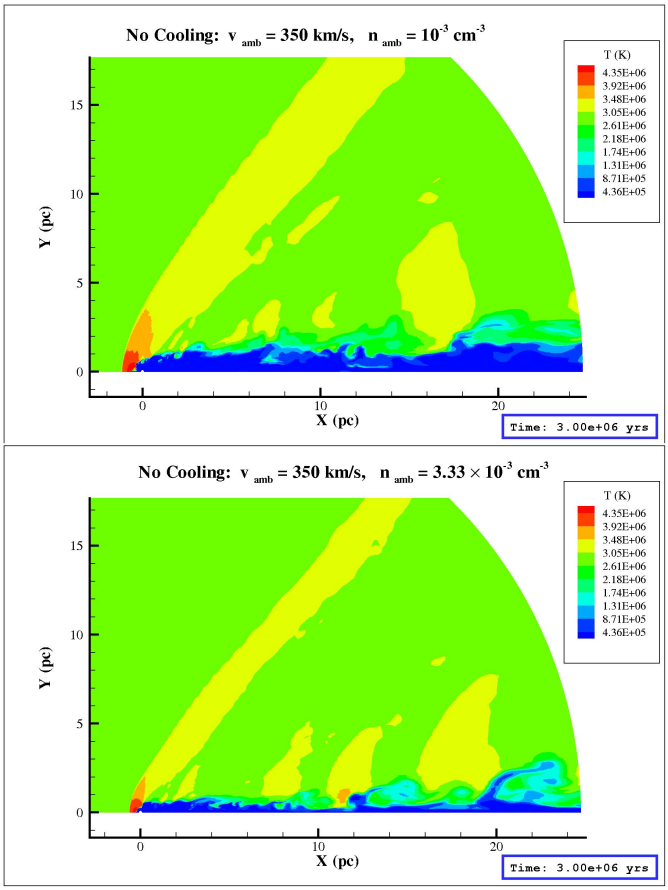

Fig. 19.— Temperature maps showing the influence of higher ambient density, at a simulation time of 3×10^6 years. The flow in the higher density simulation (bottom panel; run HDFV) occupies a smaller effective cross-section due to a higher ambient pressure, but the wake is as complex as in the fiducial (FDFV) simulation (top panel).

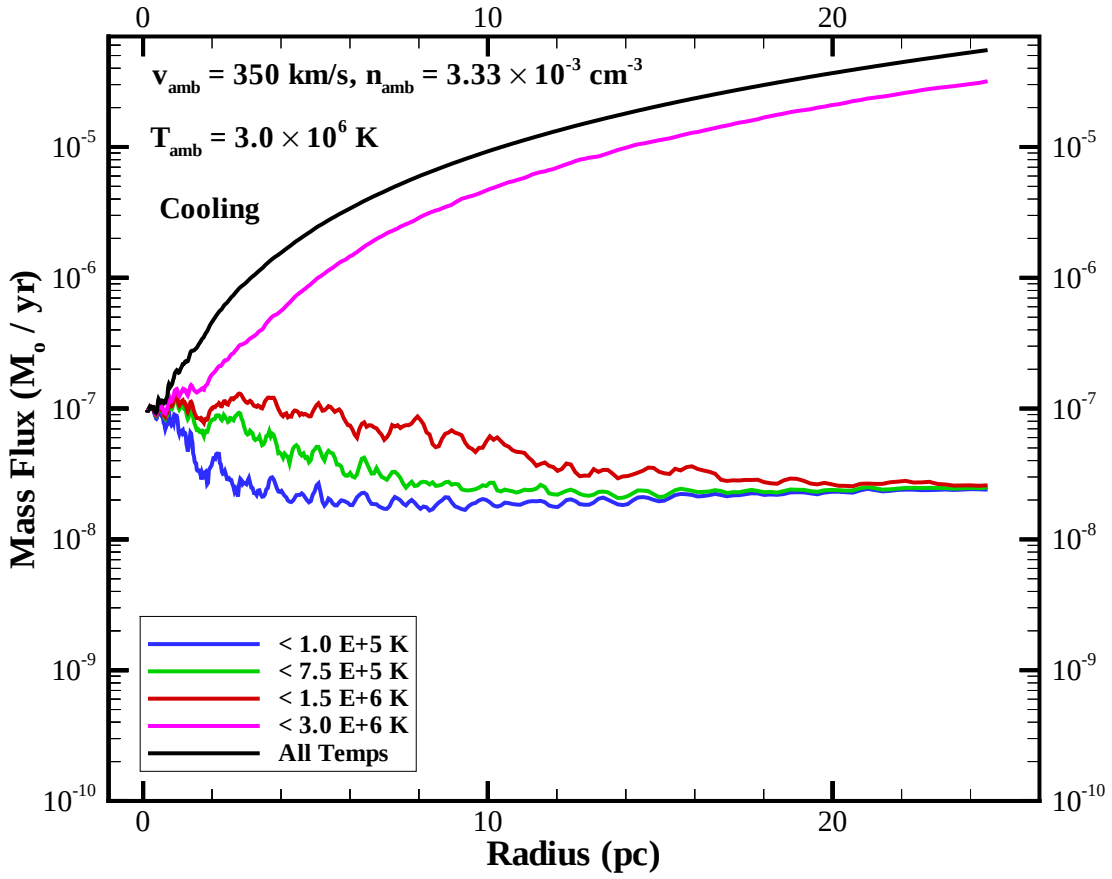

Fig. 20.— Mass fluxes for the high density simulation with cooling (run HDFVC), as a function of radius. Most of the profiles for temperature cutoffs at or below T_{amb}=2 quickly approach an asymptotic mass flux level roughly five times smaller than the stellar input value. The bulk of the heating that is accomplished by the strong bow shock and instabilities near the head of the flow. Any colder gas that survives from this region remains cool because of radiative cooling.

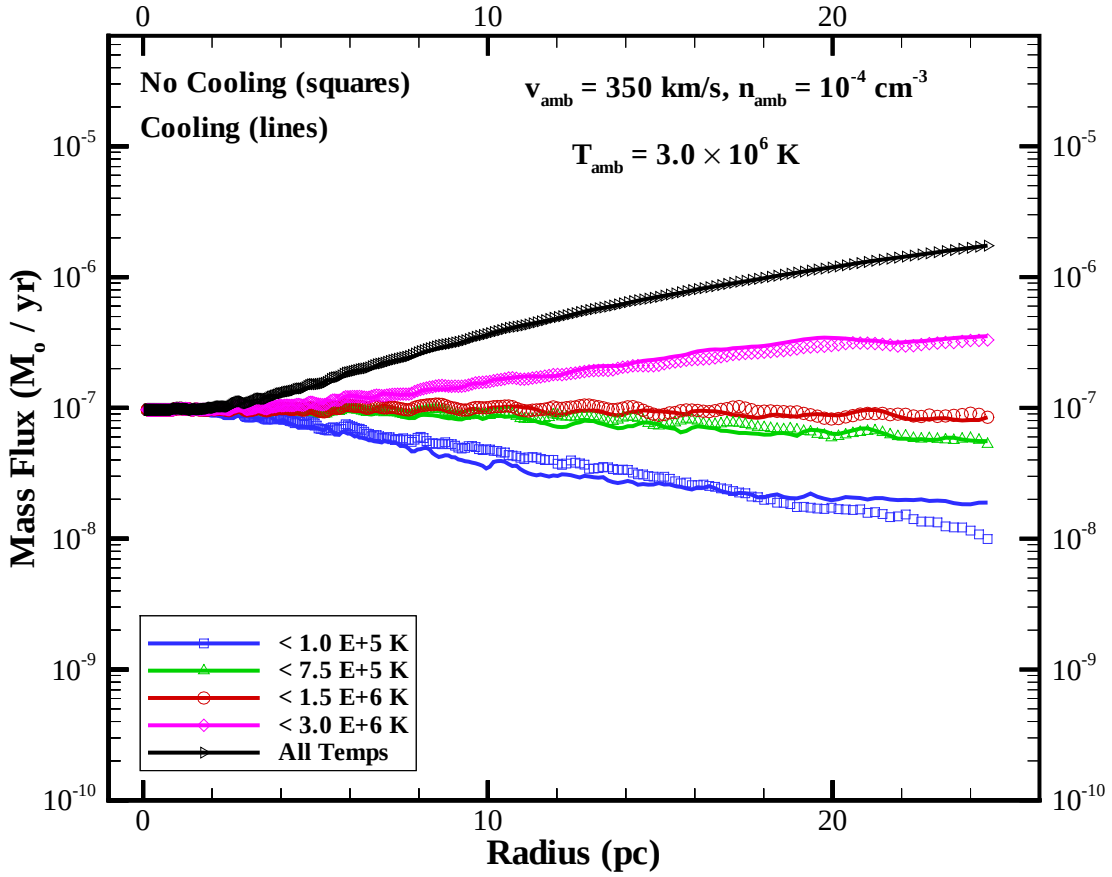

Fig. 21.— The mass flux with and without cooling for the low density simulations, LDFV and LDFVC. The long cooling times due to the low ambient density and system pressure lead to inefficient cooling, so the curves should be quite similar. However, the gas below 10^5 K appears to be approaching an steady value of about one-fifth of the initial stellar mass loss rate.

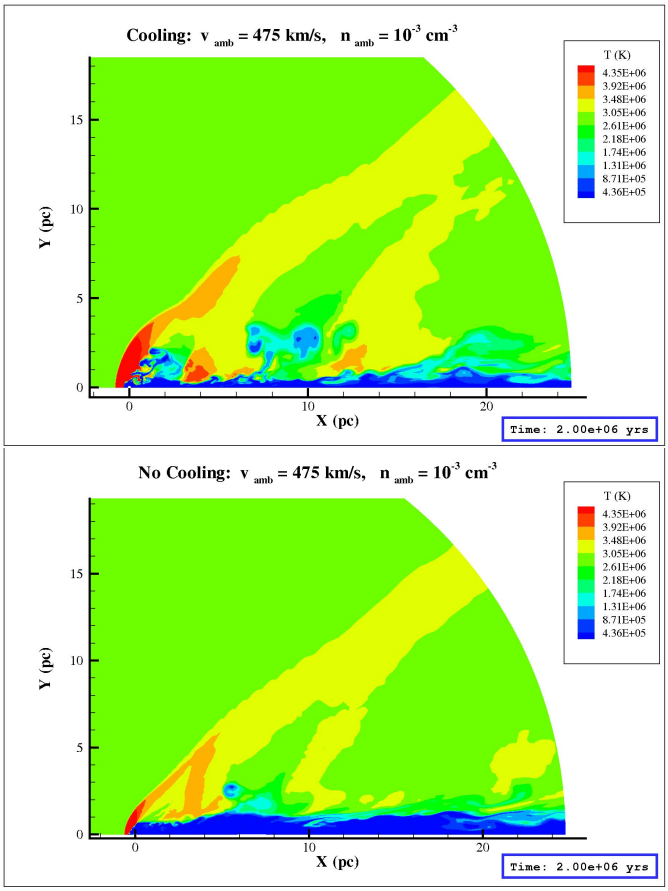

Fig. 22.— Temperature maps showing the influence of cooling on simulations with the fiducial density but high velocity (FDHV and FDHVC), at a simulation time of 2×10^6 years. The cooled flow (top panel) is more unstable than the adiabatic wake (bottom panel). Although the cooled wake is more narrow as expected, the narrower large instabilities in the cooled case are also able to survive longer against the fast wind. This in turns increases mixing.

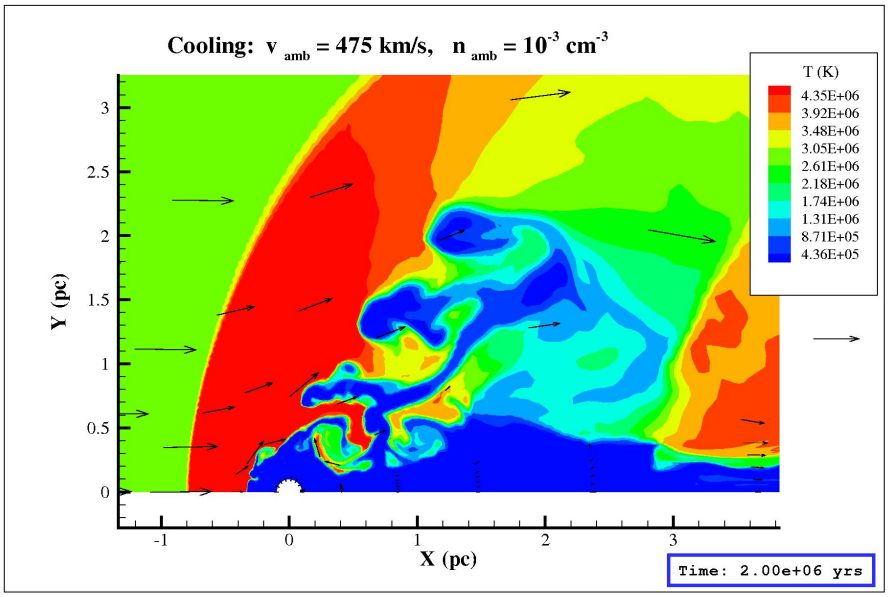

Fig. 23.— Cooled Rayleigh-Taylor fingers in the higher flow velocity simulation (FDHVC), at a simulation time of 2×10^6 years. Condensed cooled blobs have become extended and become separated due to the flow of the fast low-density material. These classical Rayleigh-Taylor fingers and the prompt mixing that accompanies them are very similar to those seen

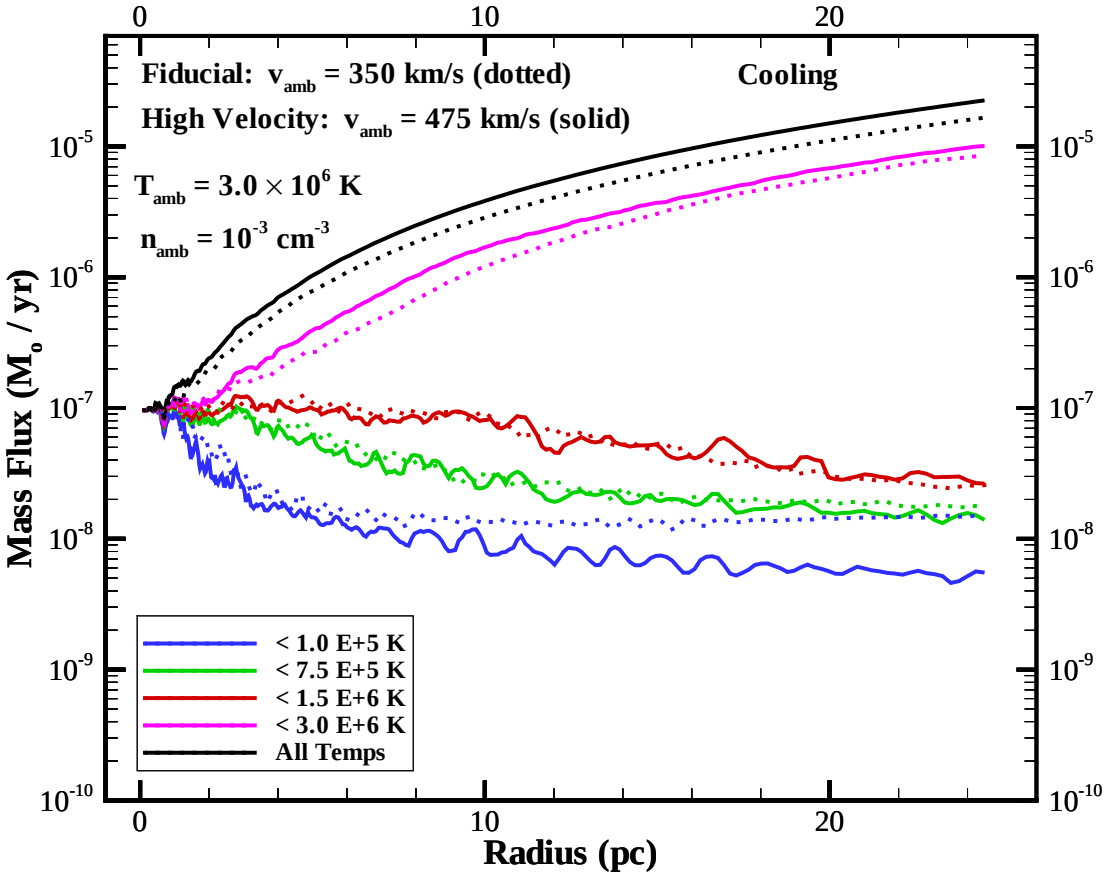

Fig. 24.— Mass flux for the fiducial and high flow velocity simulations with radiative cooling (FDHVC and FDFVC). For gas with a temperature below 3×10^5 K, the high velocity profiles (solid) lie below the fiducial velocity ones (dotted), suggesting the shock cooling time of the higher velocity case is indeed longer, and so the cooling is less efficient at lower temperatures. This difference in efficiency does not seem to apply for higher temperature gas. Also, the lack of an asymptotic convergence for the colder FDHVC profiles indicates that the accretion of warmer gas onto the narrow central cooled wake is occurring more slowly, indicating less efficient cooling.

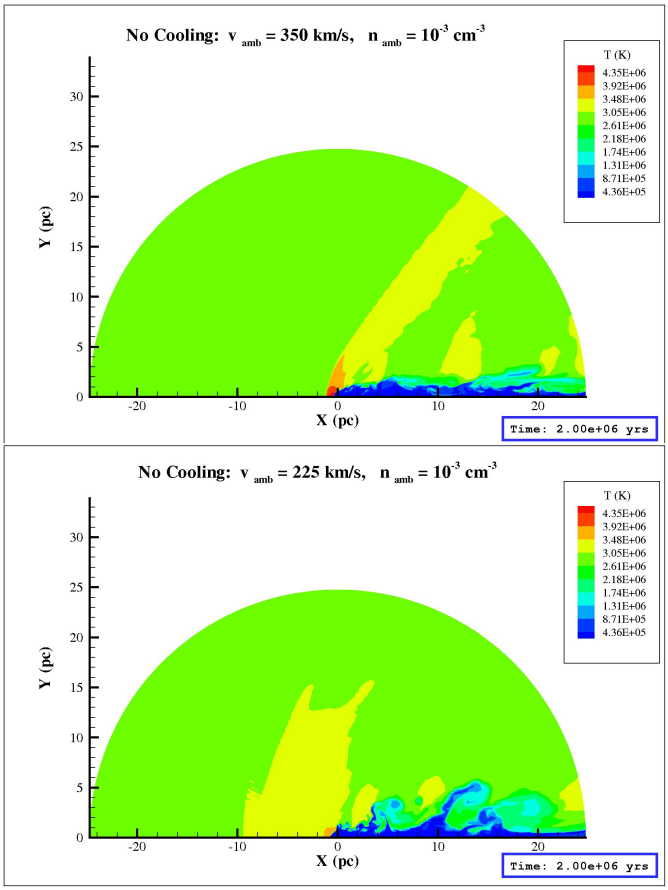

Fig. 25.— Temperature maps showing the influence of a low stellar velocity, at a simulation time of 2×10^6 years (runs FDFV and FDLV). The flow in the FDLV case (bottom panel) has similar large mode instability properties as the fiducial case (top panel; FDFV), but there are fewer small modes to aid in the wake mixing. The prominent bow shock is absent.

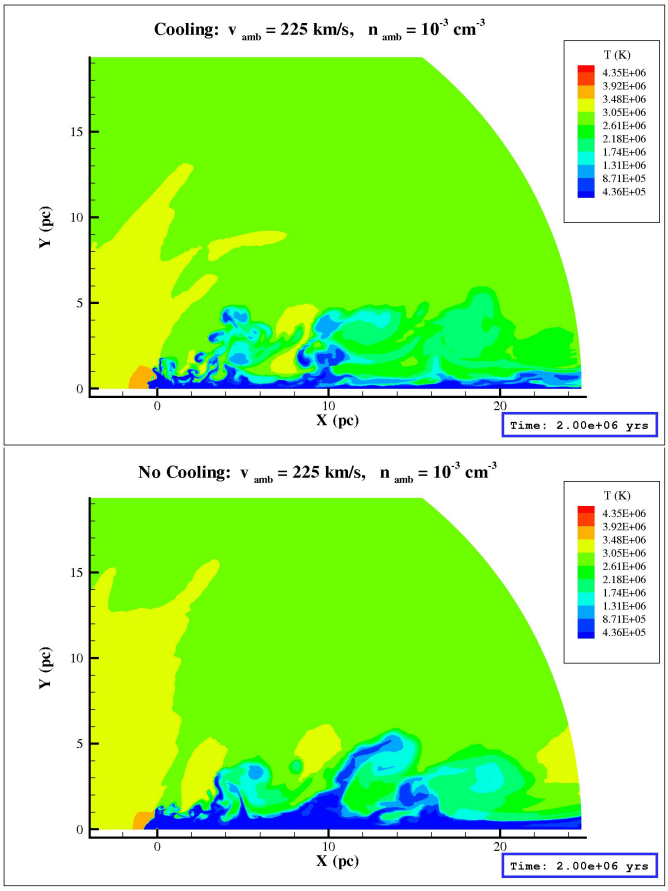

Fig. 26.— Temperature maps showing the influence of cooling on the low velocity simulations (FDLVC and FDLV), at a simulation time of 2 10^6 years. The cooled flow (top panel) is more unstable than the adiabatic wake (bottom panel). The prompt mixing by instabilities near the head of the cooled flow is once again seen in this case. The cooled wake is more narrow, as expected.

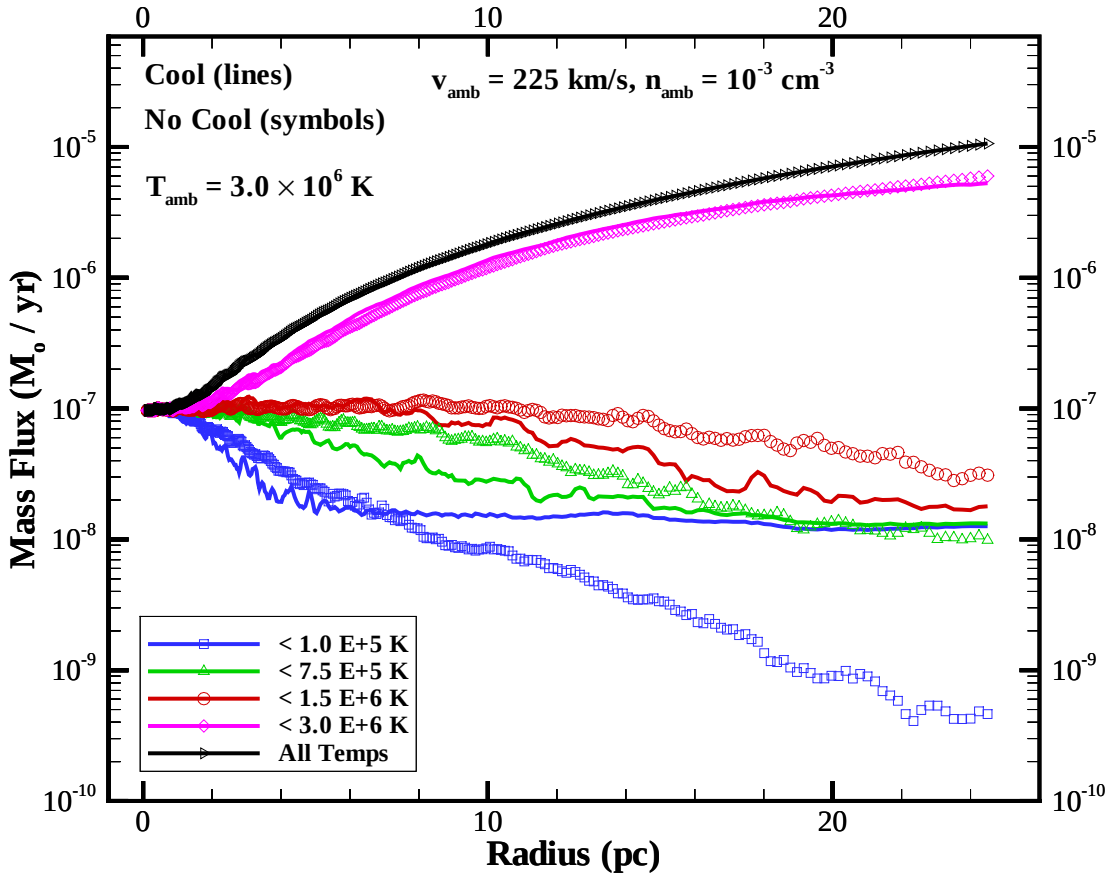

Fig. 27.— The mass fluxes in the low velocity simulations with and without radiative cooling (FDLVC and FDLV). This is very similar to the fiducial comparison. The cooled flow appears more unstable, but any stellar ejecta that escapes the heating near the head of the flow is locked into cold blobs and the narrow wake. The adiabatic wake is continuously mixed and heated in the wake as it flows downstream. The small gap between the ambient and all temperature profiles indicates that a relatively small amount of bow shock heating occurs.